Electromagnetic Scattering Model For Saline Ice Covered With Frost Flowers

by

Kulapant Pimsamarn

S.B., Massachusetts Institute of Technology (1997)

Submitted to the Department of Electrical Engineering and
Computer Science
in partial fulfillment of the requirements for the degree of   ARCHIVES

Ma   of Engineering

at the   OCT 2 9 1997

MASSACHUSETTS INSTITUTE OF TECHNOLOGY
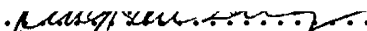
September 1997

Author . . . .
Department of Electrical Engineering and Computer Science
September 2, 1997

Certified by. . . . .
Professor Jin Au Kong
Professor of Electrical Engineering
Thesis Supervisor

Certified by . . . .
Dr. Kung-Hau Ding
Research Scientist
Thesis Supervisor

Accepted by . . . .
Arthur C. Smith
Chairman, Departmental Committee on Graduate Students

Electromagnetic Scattering Model For Saline Ice Covered With Frost Flowers

by

Kulapant Pimsamarn

Abstract

Frost flowers are saline ice crystals grown on the surface of young sea ice. The flowers are accompanied by saline slush patches underneath the ice crystals. Frost flowers have become a research interest in the study of sea ice remote sensing owing to their role in the observed enhancement of radar backscatter from thin sea ice. Various field observations have associated this increase with frost flower growth. In this thesis, based on the volume integral equation approach, an electromagnetic scattering model is developed to model the variability of microwave radar signatures with frost flower growth.

A controlled laboratory experiment (CRRELEX 1995) was carried out in 1995 to investigate relation between the C-Band polarimetric radar signatures of thin sea ice and the frost flower growth. The observed backscattering coefficients showed a nonmonotonic trend with the coverage of frost flowers on the ice surface, especially, a backscatter minimum occurred in the early stage of frost flower growth which coincided with an abrupt change in the saline ice surface salinity. The experimental measurements also suggested that the small ice crystals have little impact on the backscatter, while the slush patches yield a 3-5 dB backscatter increase over bare ice.

In the part of sea ice, a physical multilayer model is used. The salinity profiles are taken into account to derive the effective permittivity profile by using mixing formulas. For the model of frost flowers, the ice crystals are neglected due to their small contributions to the backscattering coefficients and the co-polarized ratio. The slush patches are modeled as a thin saline layer composed of an agglomeration of small square slush units of fixed thickness. An accumulation process of slush patches is developed based on a random walk algorithm to model the dynamic growth process of frost flowers.

Due to the high permittivity contrast between the slush patches and sea ice, the volume integral equation approach is used to calculate the scattered field , in which a half-space dyadic Green's function is used to take into account the coupled volume-surface interaction. In the volume integral formulation, the infinite layer approximation is used to estimate the internal field of the slush layer. A simple geometry is used to model the slush unit, and the stationary-phase method is applied to express the total scattered field as the product of the single unit's contribution and a configuration factor. The backscattering coefficients are obtained by averaging over many simulated realizations. This Monte Carlo scattering model is then applied to interpret the observed temporal variation of the polarimetric signatures of thin saline ice covered with frost flowers observed in CRRELEX 1995.

The simulation results are compared to the experimental data and match the levels of time-series data well. The scattering model produces higher σ_{vv} backscattering coefficients than σ_{hh} backscattering coefficients. The contribution of saline slush patches to the enhancement of radar backscatter is demonstrated in the simulation results. The simulation values of the co-polarized ratios or the HH-VV difference are close to the measurements. The time variation and trend of the simulation results also follow the similar trend as those of the experimental data. In addition, the simulation results show the minima which coincide with the observed minima. The observed minimum can be explained by the scattering model in terms of the difference between the surface and slush salinities.

Thesis Supervisor: Professor Jin Au Kong
Title: Professor of Electrical Engineering

Thesis Supervisor: Dr. Kung-Hau Ding
Title: Research Scientist

Contents

List of Figures

List of Tables

Chapter 1

Introduction

1.1 Background

The global climate change depends upon many factors, among which lies sea ice. The presence of ice on the ocean surface affects the air-ocean heat exchange[39]. Since sea ice covers roughly 13% of the world ocean surface during some portion of the year and interacts dynamically with the atmosphere and the ocean, changes in the thermal and geological properties of sea ice will disturb the global climate directly[13, 22]. The study of sea ice is a very active research field, as a result, many detailed measurements of sea ice properties have been carried out over the years. Those measurements include on-site, airborne, and space-borne active and passive microwave remote-sensing measurements[2]. The advantage of using microwave sensors is owing to their ability to penetrate through clouds and do not depend on the solar illumination[10].

Various electromagnetic scattering models based on either continuous or discrete random medium approaches have been developed for the study of sea ice remote sensing[38, 37, 44, 5, 11, 25]. In the continuous random medium model, the scattering comes from a random fluctuation of the medium's dielectric properties[37, 44, 25]. The fluctuation is usually described by its mean, variance, and spatial correlation

1

function[37, 44, 25]. While in the discrete random medium model, the discrete scatterers with distinct geometries are randomly imbedded in a homogeneous background medium[38, 37, 44, 5, 11]. Particles with canonical shapes such as spheres, cylinders, discs, spheroids, and ellipsoids are among the most commonly used models.

The sea ice medium is usually modeled as a multilayer random medium composed of a stack of horizontal, inhomogeneous layers of different dielectric properties and with flat or rough interfaces[5, 10]. The top half-space is air and the bottom half-space is sea water. The other layers of sea ice consists of pure ice as their backgrounds and spheroidal or ellipsoidal brine inclusions or air bubbles randomly embedded within them. The shape, size, and density distributions of the inhomogeneities could be specified to match the real physical conditions. Such a multilayer structure could be used to model both young, first-year, and multi-year sea ice. The difference between young and multi-year sea ice is that the former contains only brine pockets as the scatterers, while the latter has both brine and air inclusions embedded in ice[5, 10].

There are two important scattering mechanisms for sea ice: volume scattering from internal inhomogeneities, and surface scattering from rough boundaries between different layers. In order to accurately analyze the polarimetric radar measurements from sea ice, it is important to take into account the interaction between these two types of scattering mechanisms. Both analytic wave theory (WT) and radiative transfer theory (RT) have been applied to model microwave scattering from geophysical terrain[37]. The analytic wave theory starts from Maxwell's equations which can include the effects of multiple scattering and mutual coherent wave interactions. In general, the formulations based on the wave approach are very complicated; solutions are pursued by making approximations such as Born and/or distorted Born approximations[37, 25]. On the other hand, the radiative transfer theory is based on the energy transport equation and neglects the coherent nature of fields. How-

ever, the RT theory includes the multiple scattering effects and obeys the energy conservation[38, 37, 5, 11]. The advantage of using RT theory is that it could be applied to deal with scattering problems with much more complex geometry, such as the vegetation canopy[16], and rough or flat surface boundary conditions can be imposed at the interfaces of the layered structure[37].

Recently, an inversion algorithm for retrieving sea ice thickness based on a dynamic electromagnetic scattering model of sea ice and time-series radar measurements has been developed[40, 41, 32, 33]. This scattering model consists of a saline ice growth model, describing the dynamic variation of ice characteristics, coupled with an electromagnetic scattering model based on either analytic wave approach[40, 41] or radiative transfer method[32, 33] using a continuous random medium model[40, 41] or a discrete random medium model[32, 33]. The inversion algorithm uses a parametric estimation technique and has demonstrated an accurate reconstruction of the evolution of ice growth using the CRRELEX 93 indoor experimental data[32, 33].

1.2   Thin Sea Ice with Frost Flowers

Detection of new ice formation and ice thickness is important in understanding the dynamics of sea ice cover and the heat exchange betweenn the ocean and the atmosphere. In particular, the winter net oceanic heat input to the atmosphere through the thin ice cover can be 1 to 2 orders of magnitude greater than from parennial ice[23]. Also, the growth of new sea ice is responsible for the salinity balance in upper layers of the ocean, as well as the change of albedo of the ocean surface[12]. Therefore, the information about thin sea ice is essential, at least regionally, to the Earth's radiation budget balance.

Frost flowers occur frequently on thin sea ice cover during the Arctic and Antarctic cold season[8, 31, 19]. Frost flowers are fragile saline ice crystals which grow on the

surface of young sea ice and are accompanied by the presence of a saline slush layer under the flowers[20, 21].

Figure 1-1 shows the photograph of frost flowers grown in an indoor laboratory experiment, where the flowers densely cover the ice surface[29]. The flower ice crystals consists of thin ice platelets or needles with very high salinities[Martin & Perovich], which can grow up to a height of 10-30 mm. The thickness of the saline patch underneath the ice crystals is about 1-4 mm, which has also very high salinity[20, 29]. Their salinities are of the order of 100 practical salinity unit(psu).

In a field study on the surface of lead sea ice, Perovich and Richter-Menge[31] observed that frost flower crystals have three different morphological types: clumps, stellar dendrites, and needles, depending on air temperature, as well as the presence of highly saline skim of brine onn the ice surface. They also gave the description of the growth and decay of frost flowers. They suggested the physical mechanisms that the upward expulsion of brine from the ice interior into the flower ice crystals and the surface skims is associated with the cooling of bulk ice.

In laboratory studies of *Martin et al.*[20, 21], they described a laboratory techniques for growing frost flowers and the physical processes accompanying the growth. They found that flowers grow for the following reasons: within the ice, the thermo-molecular pressure gradient transports brine to the surface[7], where it evaporates into the cold unstable convective boundary layer. The combination of evaporation and sublimation leaves a dense brine layer at the surface and forms a region of super-saturated vapor immediately above the ice. The height of the region of supersaturated vapor in part determines the height to which the ice crystals grow[20, 21]. The other determining factor of the flower height and growth is the range of temperatures in the convective boundary layer.

Because of the associated surface salinity change, the appearance of frost flowers
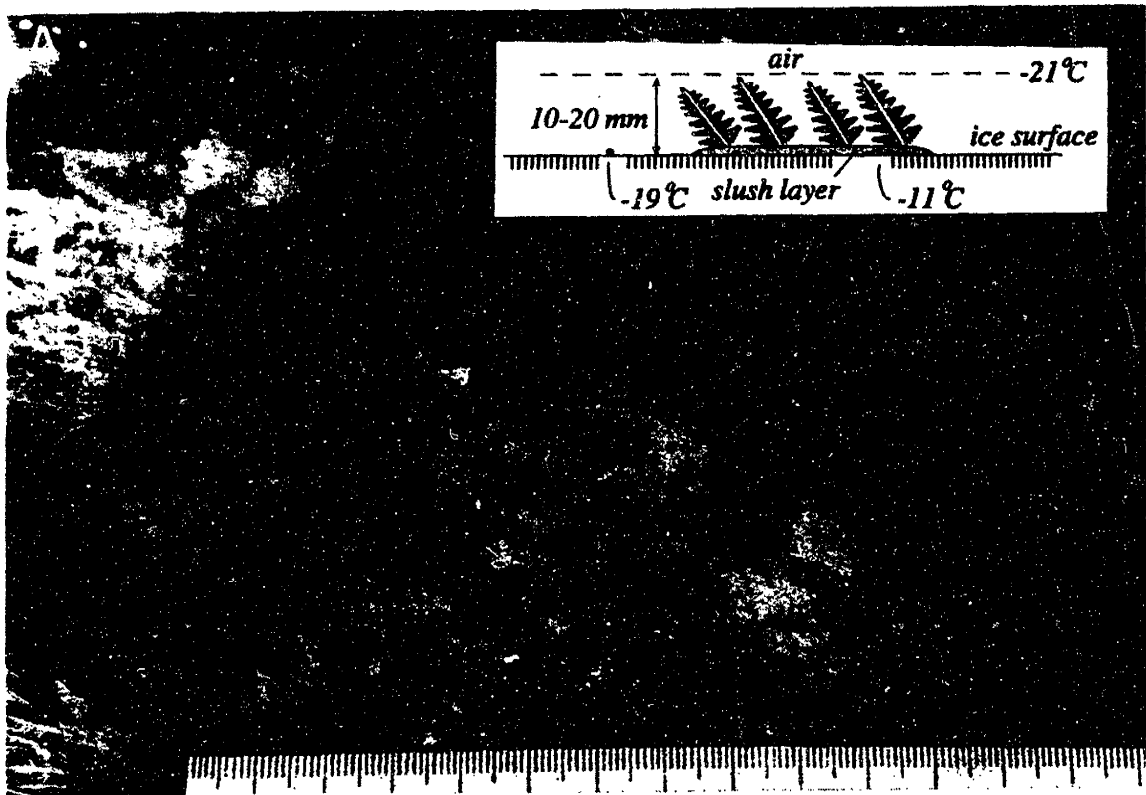
Figure 1-1: Photograph of stellar dendrite crystals taken at 9 hours. The inset shows a schematic view of the flowers, slush layer, and temperatures measured at different parts of the flowers[29].

on ice surface can have a significant impact on the microwave radar signatures of young ice. In a passive remote sensing study of thin saline ice, *Wensnahan et al.*[43] presented the temporal variations of microwave emissions from thin (0-9 cm) saline ice over a variety of frequencies (6.7,10,19,37, and 90 GHz). They observed a significant decrease in the brightness temperature at higher frequencies associated with a rapid increase in the ice surface temperature. They suggested that this is a result of the upward transport of warm brine from the interior of the sea ice to the surface. Similarly, active microwave measurements also show a distinctive variability during the early stage of sea ice growth. Hallikainen and Winebrenner[15] have associated the observed sharp increase of backscatter to young sea ice at C and X bands with either an increased ice surface roughness or the volume sca ttering from the frost flower crystals. Onstott[30] observed a backscattering increase of 12-15 dB from young sea ice which is also attributed to the frost flowers. *Ulander et al.*[39] compared backscatter values calculated from the field observations of surface properties of several young sea ice sites with ERS-1 synthetic aperture radar (SAR) observations for the same sites. A backscatter increase of 5-10 dB is observed, with the largest increase occurring for snow-infiltrated flowers. Field observations also suggested that the flower formation makes the ice appear brighter to microwave backscatter. An increase of approximately 6 dB associated with the young ice growth is observed from the ERS-1 SAR images of a lead in the Beaufort Sea[29]. *Nghiem et al.*[29] suggested that frost flowers are the cause of the enhanced radar backscatter.

A laboratory study on C-band radar backscatter from frost flowers on saline ice was conducted, during February 1995 (CRRELEX 1995)[29], to investigate the variability in the radar signatures accompanied with the growth of frost flowers. The experimental results suggested that the strong C-band radar backscatter increase of the order of 5 dB, over the background radar return from thin bare ice, can be used

as an index to mark the nearly full coverage (90% areal coverage) of frost flowers.

1.3   Description of Thesis

The second chapter is dedicated to the controlled experiment which provides times-series measurements of the physical conditions and the actual backscattering coefficients. The thesis, strictly based on the experiment, will proceed with the construction of the electromagnetic scattering model for sea ice covered with frost flowers. So, the attempt is made to model the whole scattering picture piece by piece starting with sea ice in Chapter 3, where the model of sea ice is introduced based on the actual physical properties of sea ice which has shortly discussed in Chapter 1. Decisions about the physical model is given suporting evidence. The third chapter also includes the modeling of the slush layer where it is plausible that the ice crystals are neglected. It also includes how to randomly create various realizations for the model average calculation, which are crucial parameter specifications.

Accordingly, the scattered field is calculated in Chapter 4 by the volume integral equation approach in combination with the infinite-layer approximation to estimate the internal field of the slush layer. The solution is however simplified for computational purposes by engaging the method of stationary phase; the computation aspect of the Monte Carlo simulation is implied. The total scattered field is derived from a single slush unit contribution, where the same slush unit is used for the simulation of frost flower growth, since the volume integral calculation for the whole slush layer takes an extremely large amount of time. Then, the calculation of backscattering coefficients with the simulation parameters derived from the frost flower experiment, which is discussed in Chapter 2, appears in Chapter 5. Moreover, the simulation results are also compared to the experimental observations in the same chapter. Eventually, the thesis is summarized in the last chapter.

Chapter 2

Laboratory Investigations on Radar Backscatter from Frost Flowers on Saline Ice

Frost flowers form frequently on thin sea ice during the Arctic cold season, which account for the enhanced radar backscatter from young sea ice[29]. During February 1995, Jet Propulsion Laboratory (JPL), University of Washington (UW), Cold Regions Research and Engineering Laboratory (CRREL), and Massachusetts Institute of Technology (MIT) conducted a series of laboratory experiments on saline ice in an indoor cold room at CRREL to investigate the effect of frost flower growth on the C-Band polarimetric radar response from the sea ice and to identify radar characteristics of thin sea ice covered with frost flowers[28]. In this chapter, the evolution of measured C-band polarimetric backscatter signatures and the physical characteristics of the growth of frost flowers on saline ice are briefly described and discussed. The detailed experimental setup, procedures, and findings have been reported by *Nghiem et al.*[29].

2.1 Description of The Experiment

The frost flower experiments were performed in an indoor cold room, which is a two-story refrigerated facility called "the Pit", at CRREL. The air temperature in the room could be controlled to within $2°C$. A freezing pool in the lower level was used to grow the ice. The pool was filled with a volume of sodium chloride solution of 31 practical salinity units (psu) to a 90cm depth. In fact, it has been shown that the laboratory sodium chloride ice and the sea ice in Arctic have similar characteristics in their growth rates, temperature profiles, salinity profiles, brine volumes, desalination effects, crystallographic structures, and intercellular spacings for the thickness of young ice under consideration[1, 26].

The C-band (5 GHz) polarimetric radar system was set on the upper floor of the cold room. The antenna aperture was in the far field about 3 m away from the sea water pit on the lower floor. The antenna was put inside an anechoic enclosure to treat the multipath problem. Anechoic absorbers were also used to cover the wall and the floor. The controlling system of the polarimetric scatterometer was outside the cold room where all system operations were done including RF control, polarization switching, antenna pointing, and data acquisition. The setup allowed the antenna to be pointed at any incident and azimuthal directions. The video camera looked normally downward to the ice surface at the field of view (FOV) covering the surface area of 0.5m×0.5m. Lamps were attached to the sides of two catwalks alongside the water pit for the video lighting. Additional absorbers were used to shield the video system and the catwalks together with the lamps were also covered with absorbers such that unwant ed reflections and multipath effects had the least influence in radar measurements. Another computer setup was also outside the cold room to take time-series images of the frost-flower growth. A thermistor string was submerged into water from the beginning of the ice growth to obtain the temperature profile data.

The room temperature was lowered to $-28°C$ to initiate the ice growth. Once the saline ice sheet started to form, the physical characteristics of ice and flower and radar backscatter were measured at 6- to 12-hour intervals throughout the experiment. Ice characterization measurements include the thickness of ice and slush layer and the salinities of frost flower, slush layer, and the adjacent bare ice. Data for air temperature, ice surface temperature, water temperature, and approximate thickness of the humidity layer were also collected. Besides the video recording of frost flower growth, closeup photographs of frost flowers were also taken.

This frost flower experiment lasted about 3 days, during which time the ice thickness grew to a 15-cm thickness and the water salinity increased from approximately 31 to 35 psu. At the termination of the experiment, the flower areal coverage seemed to reach what appeared to be its final coverage.

2.2   Experimental Measurements

2.2.1   Frost Flower Observation

The ice sheet was grown from open water without seeding. The air temperature was kept between $-29°C$ and $-28°C$, which was a favorable condition for the growth of frost flowers[20]. At an ice thickness of 1 cm, some frost flowers started to appear on the surface of the ice. The flowers began as individual small crystals with no slush underneath. As crystals grew laterally into clusters, the slush layer, which is the basal area under the crystals, formed and increased in thickness beneath the flowers. In contrast, the slush layer did not exist on the bare ice surface outside the flower clusters. During the first day, the growth of frost flowers was slow and the areal coverage was less than 20%. The flower growth rate increased during the second day and more than 85% flower coverage was achieved. At the end, the frost

10

flower formation covered 90% of the ice surface. The frost flowers were composed of dendritic ice crystals and were about 10-20 mm high. The slush layer th ickness was about 2-4 mm. It was also found that the air temperature at the top of the flowers was approximately $-21°C$, and the temperature below the flowers within the slush layer was approximately $-11°C$. Although the flower top temperature was lower, the slush layer temperature is consistent with dendritic flower growth[29].

Later in the experiment, the dendrites were observed to transform slowly into needles. The needles had a length of 10 mm and a diameter of less than 1 mm. The change of frost flower crystal during its growth is due to the ice surface temperature decreases as the ice thickness increases[14]. This decrease in ice surface temperature with increasing thickness means that the initial conditions favor dendritic crystals and that needles form later. Additionally, the inset measurements showed that the needles had a temperature of $-17°C$ at the top of the slush layer and a temperature of $-25°C$ at the top of the flowers. Compared with the higher temperature of the dendritic flower crystals, it suggests that the transition from dendrites to needles is associated with the cooling of the ice surface caused by the increase in ice thickness. In addition, the ice surface temperature under the slush layer was observed to be about $8°C$-$10°C$ warmer than the temperatures of the a djacent bare ice, the cause of this is the insulating effect of frost flowers[21].

The time-series photographs of frost flowers on saline ice illustrating the stages of frost flower growth[29] are shown in Figure 2-1. The percentage areal coverage was obtained from the digitized images[29]. Figure 2-2 (a) shows the evolution of ice thickness during the 3-day growth, and Figure 2-2 (b) shows the corresponding areal coverage of frost flowers on the ice surface. The decrease of bulk ice salinity is plotted in Figure 2-2 (c), which is due to the desalination effect. The circles in Figure 2-2 represent the measurement data[29]. From Figure 2-2, we can see that as the areal

coverage of frost flowers increases from 0 to 90%, the ice thickness grows from 5 to 15cm, and the bulk salinity drops from 15 to 11 psu.

The physical characterizations of saline ice also include the time-series measurements of the salinities of ice surface, frost flower, and slush layer, which are shown in Figures 2-3 (a), (b), and (c), respectively. Figure 2-3 (a) shows a high leap in the surface salinity occurred around the 32nd hour. However, during this time period of growth, generally, both flower salinity and slush salinity increase with time.

2.2.2 Radar Backscatter Measurements

Throughout the ice growth with increasing frost flower coverage, fully polarimetric C-band backscatter data were taken at incident angles ranging from 0° to 45°. At each incident angles, data were collected at all linear polarization combinations of transmitted and received signals with 401 frequency points, 20 time coherent averaging, and 4 different azimuthal angles for independent sampling[28].

Figures 2-4 (a) and (b) present the measured backscattering coefficients, σ_{HH} and σ_{VV}, versus the elapsed time at two different observation angles 25° and 35°, respectively. As shown in Figure 2-4, both vertical and horizontal backscattering coefficients increase with time, hence the flower coverage and the ice thickness, until a minimum occurs at about the 35th hour[29]. A cross examination with Figure 2-3 (a) shows that the time of the backscatter minimum coincides with the time at which an abrupt change happened in the ice surface salinity. The backscattering return is higher for the smaller observation angle because of a longer attenuation path through the frost flower constituents at a larger observation angle.

In order to determine the contributions of slush patches to the radar polarimetric signatures, three sets of backscatter data, at the final stage of frost flower growth were taken from ice first, with all constituents of frost flowers included, then with
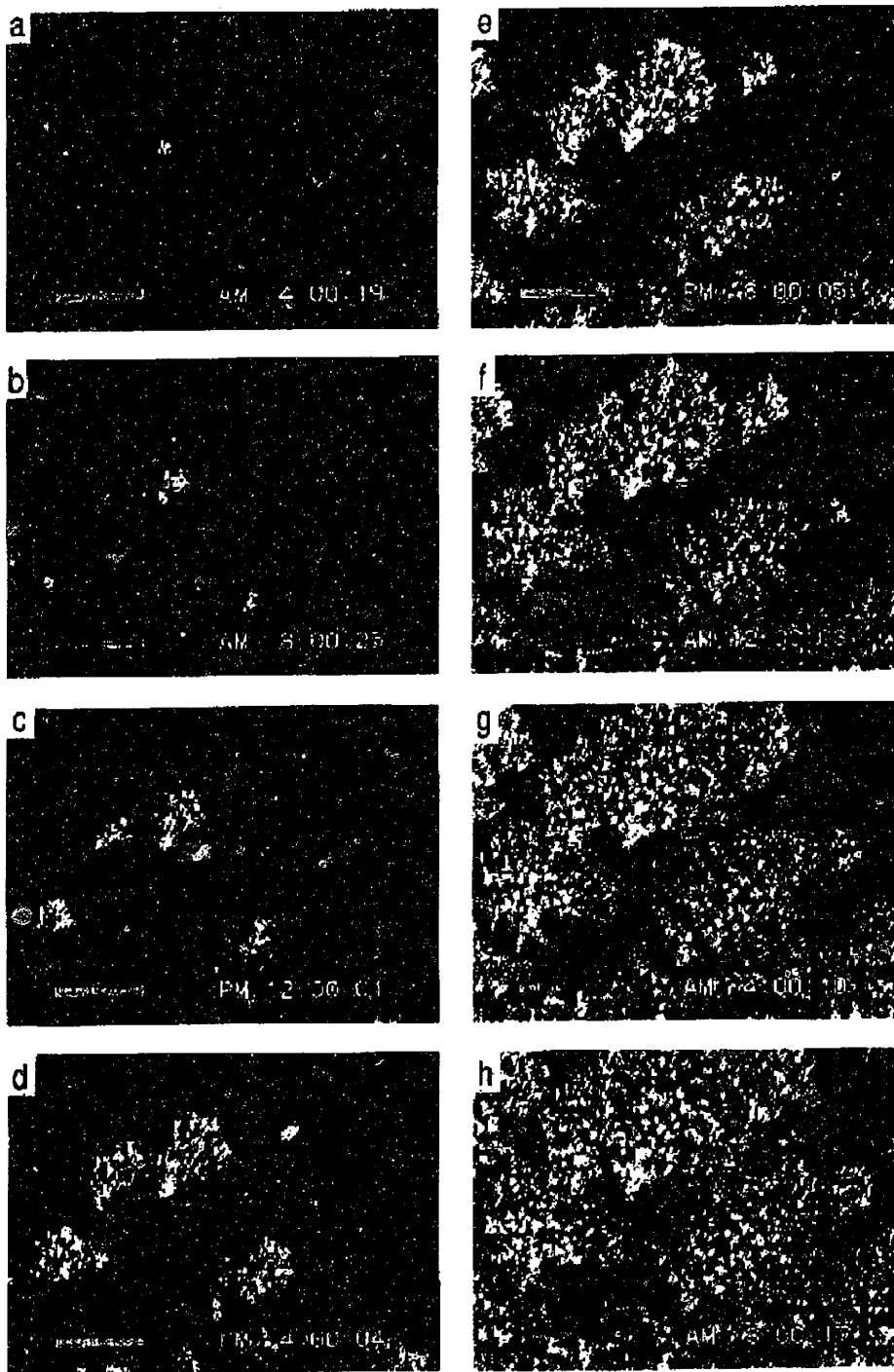
Figure 2-1: Sequence of video images showing the growth of frost flowers at 4-hour intervals starting at 0400 local time, which corresponds to an elapsed time of 16 hours. The 10-cm ruler shown at the lower left position provides a scale for the images.[29]
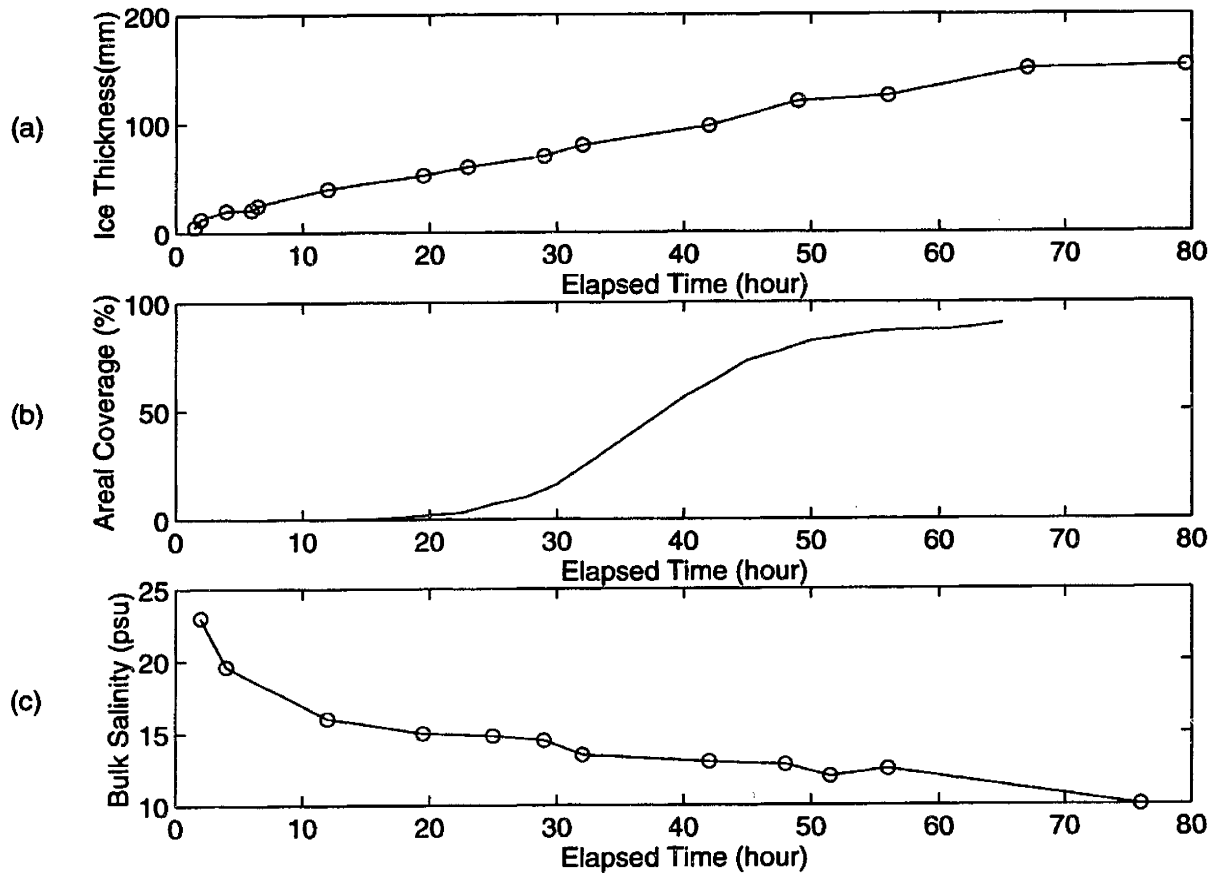
Figure 2-2: Time-series measurements of (a) the ice thickness, (b) the areal frost flower coverage, (c) and the ice bulk salinity.
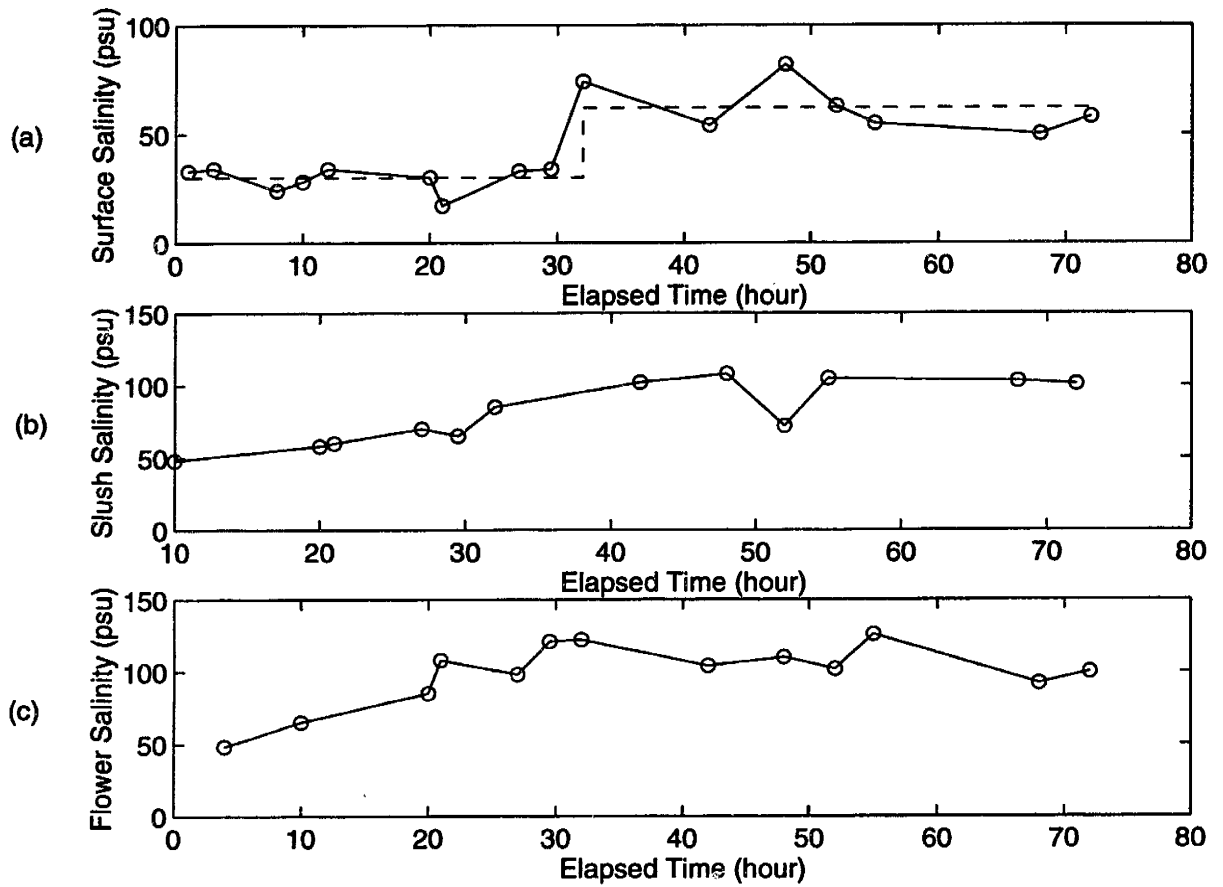
Figure 2-3: The time-series measurements of the salinities of (a) the bare ice surface, (b) the frost flowers, and (c) the slush patches.
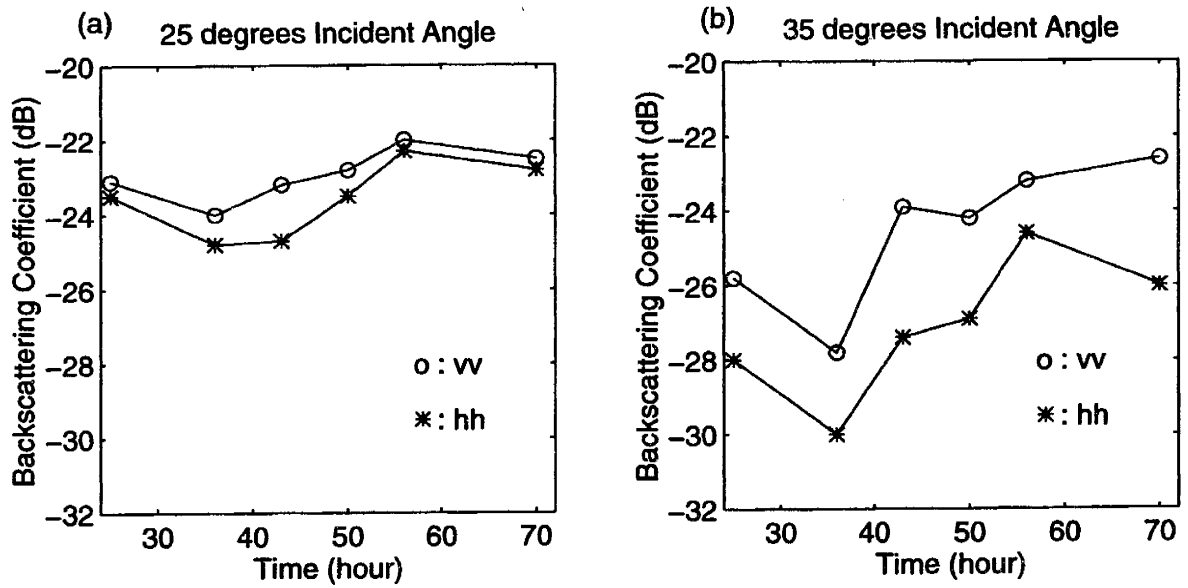
Figure 2-4: Backscattering coefficients: (a) 25° incident angle, and (b) 35° incident angle, of saline ice covered with frost flowers from CRRELEX 1995[29]. Circles are backscatter data for σ_{vv} and asterisks are backscatter data for σ_{hh}.

the fluffy ice crystals removed, and finally with all the slush patches taken away. Tables 2-1 and 2-2 compare the backscattering coefficients and the co-polarized ratio, $\gamma = \frac{\sigma_{vv}}{\sigma_{hh}}$, respectively, at two incident angles of 25 and 35 degrees, for the ice with full frost flowers (90% areal coverage), for the ice with slush patches exposed but without ice crystals, and for the bare ice with all slush patches removed. The difference of backscatter between the with full frost flowers and the ice with slush patches only was less than 2 decibels.

From Table 2.1, it is found that the case of ice with slush patches exposed gives the highest backscattering return, and the difference is around 1 dB compared to that prior to the removal of ice crystals. The lower return for the case of full frost flowers is due to the attenuation caused by the lossy fluffy ice crystals. Bare ice without frost flowers, however, results in the lowest backscattering coefficients. This suggests that the flower ice crystals contribute little to the C-band microwave backscatter because of their small sizes. The higher radar return with the full frost flower cover compared to that of bare ice accounts primarily for the enhanced radar backscatter observed in SAR images.

Ice Covering	25°		35°	
	σ_{vv}	σ_{hh}	σ_{vv}	σ_{hh}
Full Frost Flowers	-22.4	-22.7	-22.7	-26.0
Slush Patches	-20.8	-21.8	-22.0	-24.8
None(Bare Ice)	-25.2	-25.8	-26.9	-28.4

Table 2.1: Comparisons of backscatter σ_{vv} and σ_{hh}, at two angles of 25° and 35°, for the full frost flower formation(about 90% in areal coverage), for slush patches exposed by removing flower ice crystals in the frost flower formation, and for the bare ice with all slush patches removed.

Ice Covering	25°	35°
	σ_{vv}/σ_{hh}	σ_{vv}/σ_{hh}
Full Frost Flowers	0.25	3.4
Slush Patches	1.0	2.8
None(Bare Ice)	0.5	1.6

Table 2.2: Comparison of co-polarized ratio between the horizontal and vertical returns at two angles of 25° and 35°. These are for the full frost flower formation (about 90% in areal coverage), for slush patches exposed by removing flower ice crystals, and for the bare ice with all slush patches removed.

Chapter 3

Physical Model of Saline Ice Covered with Frost Flowers

According to the experimental observations described in Chapter 2, the contribution flower crystals to the C-band radar backscatter is much smaller compared to the contribution from the slush layer. Therefore, the following development of the electromagnetic scattering model for saline ice covered with frost flowers, the focus will be on the modeling of scattering from slush patches. However, the growth of flowers is a dynamic process, a viable model must accompany a reliable and plausible frost flower growth process which can artificially generate desired areal coverages with random appearance of slush patches. For this purpose, a growth process based on random walk is used to generate realizations of slush patches on top of ice surface. To avoid any preferred configuration, an ensemble of realizations for each slush coverage will be created to perform the configuration average. This Monte Carlo simulation approach will be used in Chapter 5 to compute backscattering coefficients. In the following, the models of sea ice and slush patches are described in connection with the invented growth process thereafter.

3.1   Multilayer Model of Sea Ice

In this study, the scattering from brine pockets within the saline ice is neglected. The sea ice is modeled as a stack of homogeneous horizontal layers with a finite thickness. The effective permittivity of each ice layer is determined from empirical formulas which will be described briefly in the following. The well-known C-shaped salinity profile of sea ice[42, 24, 9] is taken into account in the computation of effective sea ice permittivity. A quadric polynomial will be used to simulate the salinity profile based on the measured surface and average salinities.

A linear temperature profile is also assumed within the sea ice layer[42]. Figure 3.1 shows the schematic diagram of a slush patch on top of the sea ice surface with the distribution of temperature and salinity within the ice. The uppermost medium is air with permittivity ϵ_0 and the lower half space is saline water with complex permittivity ϵ_w.

The sea ice layer and sea water beneath the frost flowers all affect the overall electromagnetic interactions with sea ice. Both brine inclusions within the ice layers and the rough interfaces contribute to the backscatter. Another contribution is from the coupled volume and surface interactions where the reflection property of the boundary between air and ice plays an important role in determining the internal fields of slush patches. However, in the development of the scattering model, the complexities of scattering by rough interfaces and brines are neglected. The validity of this model will be demonstrated by comparison with the experimental data.

3.1.1   Modeling of the Salinity Profile

The salinity profile within the ice is assumed to be only dependent upon the depth from the surface. This assumption is equivalent to assume that the positions of brine pockets are uniformly distributed in the horizontal directions of the sea ice layer.

21

Figure 3-1: The schematic diagram of the C-shaped salinity profile and the linear temperature profile within the sea ice at each layer. A slush patch is shown on the sea ice surface.

Salinity profiles in thinner ice tend to be C-shaped[42]. Moreover, the mere information about the surface and bulk salinities, which were measured in the experiment, does not allow much flexibility of viable profiles. The functional form of the model salinity profile contains at most two unknowns which can be determined from the measured salinities. Furthermore, since the profile is expected not to be too fast-varying, we choose low-order polynomial to model the salinity profile. Let $s(\xi)$ be the salinity as a function of the depth ξ, the salinity profile is assumed of the following form:

$$s(\xi) = a_4(\xi - \xi_0)^4 + a_0 \qquad (3.1)$$

where ξ_0 is the depth at which the salinity profile has its minimum, and $a_0(\text{psu})$ and $a_4(\text{psu}/m^4)$ are the expansion coefficients. It is noted that there are three unknowns, ξ_0, a_0, and a_4, in the model profile of (3.1) , which have to be determined from the measured surface and average salinities. It leaves ξ_0 to be an adjustable parameter to give the best matched results while most other parameters are settled.

Let

$$s(0) = s_{surface} \qquad (3.2)$$

$$< s >_\xi = s_{bulk} \qquad (3.3)$$

, where $s_{surface}$ and s_{bulk} are the measured surface and bulk salinities respectively. The average $< s >_\xi$ can be expressed as

$$< s >_\xi = \frac{\int_0^d d\xi s(\xi)}{d} \qquad (3.4)$$

where d is the thickness of the sea ice. Substituting (3.1) into (3.4) , we get

$$< s >_\xi = a_0 + \frac{a_4}{5}(d^4 - 5d^3\xi_0 + 10d^2\xi_0^2 - 10d\xi_0^3 + 5\xi_0^4) \tag{3.5}$$

From (3.2) , (3.3) , and (3.5) , a_0 and a_4 can be solved in terms of ξ_0.

$$a_0 = s_{surface}\left(\frac{d^4 - 5d^3\xi_0 + 10d^2\xi_0^2 - 10d\xi_0^3 + 5\xi_0^4}{d^4 - 5d^3\xi_0 + 10d^2\xi_0^2 - 10d\xi_0^3}\right)$$
$$-s_{bulk}\left(\frac{5\xi_0^4}{d^4 - 5d^3\xi_0 + 10d^2\xi_0^2 - 10d\xi_0^3}\right) \tag{3.6}$$

$$a_4 = \left(\frac{5(s_{bulk} - s_{surface})}{d^4 - 5d^3\xi_0 + 10d^2\xi_0^2 - 10d\xi_0^3}\right) \tag{3.7}$$

This salinity profile will be applied in determining the effective permittivities of sea ice layers.

3.1.2 Modeling of the Dielectric Property of Sea Ice

The young sea ice is a mixture of pure ice and brine inclusions, and its effective complex dielectric constant is a weighted average of the complex dielectric constants of the constituent components[37]. Throughout the range of microwave frequencies, the complex dielectric constant of pure ice is almost invariant[38]. The real part of the dielectric constant is around 3.2 and imaginary part is quite small.

Effective Dielectric Constant of Saline Water

To compute the complex dielectric constant of saline water, an equation of the Debye form has been developed[35]

$$\epsilon_r = \epsilon_\infty + \frac{\epsilon_s - \epsilon_\infty}{1 - i2\pi f\tau} + i\frac{\sigma}{2\pi\epsilon_0 f} \tag{3.8}$$

where ϵ_r is the relative complex dielectric constant of saline water, ϵ_s and ϵ_∞ are

the static and high frequency relative dielectric constants of the saline water, τ is the relaxation time, f is the frequency, σ is the ionic conductivity of the dissolved salts, and ϵ_0 is the permittivity of free space. The ionic conductivity is assumed to be independent of the frequency[35, 17]. In [35], a series of simple polynomial fits to real measured permittivity for saline water have been given for the four parameters ϵ_s, ϵ_∞, τ, and σ, each of which is a function of the temperature only. According to [35], the constants are

$$\sigma = \begin{cases} -te^{0.5193+0.08755t} & t \geq -22.9^\circ C \\ -te^{1.0334+0.1100t} & t < -22.9^\circ C \end{cases} \tag{3.9}$$

$$\epsilon_s = \left(\frac{939.66 - 19.068t}{10.737 - t}\right) \tag{3.10}$$

$$\epsilon_\infty = \left(\frac{82.79 + 8.19t^2}{15.68 + t^2}\right) \tag{3.11}$$

$$\tau = \left(\frac{1.0990 10^{-10} + 1.3603 \times 10^{-12}t + 2.0894 \times 10^{-13}t^2 + 2.8167 \times 10^{-15}t^3}{2\pi}\right) \tag{3.12}$$

As the ice changes temperature, internal melting or freezing within the brine inclusions affect the brine volume of the ice. Cox and Weeks[6] developed an expression which gives the fractional volume of brines, f_b, in sea ice as a function of its temperature and salinity.

$$f_b = \left(\frac{\rho_i S_i}{F_1(t) - \rho_i S_i F_2(t)}\right) \tag{3.13}$$

where S_i is the salinity of the ice (ppt), t is the temperature in $^\circ C$, and for $-2^\circ C \geq t \geq -22.9^\circ C$,

$$F_1(t) = -4.732 - 22.45t - 0.6397t^2 - 0.01074t^3 \qquad (3.14)$$

$$F_2(t) = 0.08903 - 0.01763t - 5.33 \times 10^{-4}t^2 - 8.801 \times 10^{-6}t^3 \qquad (3.15)$$

$$\rho_i = 0.917 - 0.0001403t \qquad (3.16)$$

In the expression (3.13) , the fractional volume of air in ice has been neglected.

Effective Dielectric Constant of Sea Ice

Assuming the brine pockets to be randomly oriented ellipsoids, the effective permittivity of sea ice, ϵ_{eff}, can then be calculated using Polder-van Santen mixing formula[34]

$$\epsilon_{eff} = \epsilon + \frac{f}{3}(\epsilon_s - \epsilon) \sum_{i=1}^{3} \frac{\epsilon_{eff}}{\epsilon_{eff} + N_i(\epsilon_s - \epsilon_{eff})} \qquad (3.17)$$

here ϵ is the complex permittivity of ice, ϵ_s is the permittivity of brine inclusions, f is the fractional volume of brines, and N_i is the depolarization factor of brine particles

$$N_i = \int_0^{\infty} ds \frac{a_i a_j a_k}{2(s + a_i^2)^{\frac{3}{2}}(s + a_j^2)^{\frac{1}{2}}(s + a_k^2)^{\frac{1}{2}}} \qquad (3.18)$$

with a_1, a_2, and a_3 being the semi-axes of an ellipsoidal particle. Equation (3.17) is solved self-consistently to obtain ϵ_{eff}.

3.1.3   Reflection Coefficients of Stratified Sea Ice Medium

The reflection coefficient for the infinite medium with an arbitrary continuously-varying permittivity profile is difficult to evaluate. However, the formula for calcu-

lating reflection coefficients from a stratified medium is well documented. Hence, in the sea-ice model, we approximate the continuous profile by a piecewise constant profile consisting of layers of constant permittivity. Therefore, sea ice can be viewed as comprising homogeneous layers of certain fixed permittivities.

Since, with the salinity and temperature profiles, the permittivity can be calculated at any depth, we know the permittivity profile in any layer in the multilayer model. The permittivity still continuously varies within each layer. Therefore, to use the homogeneous layers for simulation calculations, the permittivity assigned to a layer is the average of the permittivities at the two end surfaces of the layer.

Figure 3-2 illustrates the dielectric model of sea ice. As indicated, the salinity and temperature profiles are discretized. This amounts to a stack of homogeneous layers with constant permittivities.

Consider a plane wave incident on a stratified isotropic medium with boundaries at $z = -d_0, -d_1, \cdots, -d_n$ in Figure 3-3. The layer between the mth and the (m+1)th regions is the plane $z = -d_m$. The (n+1)th region is semi-infinite and is labeled as region t. The permittivity and permeability in each region are denoted by ϵ_l and μ_l. The plane wave is assumed to be incident from the region 0. Note that, without loss of generality, all field vectors are assumed independent of y. That is, the partial derivative with respect to y, $\frac{\partial}{\partial y}$, always vanishes for each vector entity.

The ratio, $R_l = \frac{A_l}{B_l}$, between the amplitude of the upward-going wave amplitude and that of the downward-going wave is[18]

$$R_l = \frac{e^{2ik_{lz}d_l}}{R_{l(l+1)}} + \frac{\left(1 - \frac{1}{R_{l(l+1)}^2}\right)e^{2i(k_{(l+1)z}+k_{lz})d_l}}{\frac{1}{R_{l(l+1)}}e^{2ik_{(l+1)z}d_l} + R_{(l+1)}} \tag{3.19}$$

where $R_{l(l+1)} = \frac{1-p_{l(l+1)}}{1+p_{l(l+1)}}$, and $p_{l(l+1)} = \frac{\mu_l k_{(l+1)z}}{\mu_{(l+1)}k_{lz}}$, for TE waves. Duality gives similar results for TM waves.

R_0 is the TE reflection coefficient for plane waves traveling downwards from region
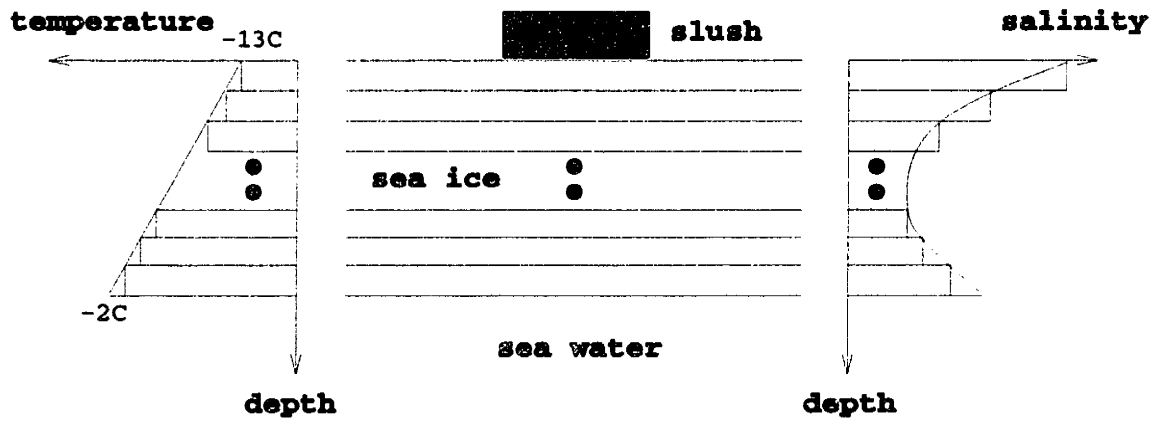
Figure 3-2: The dielectric model of sea ice where the salinity profile relates to the permittivity through a formula.

z

x

Region 0

Region 1

Region 2

●

●

●

Region n

Region t=n+1
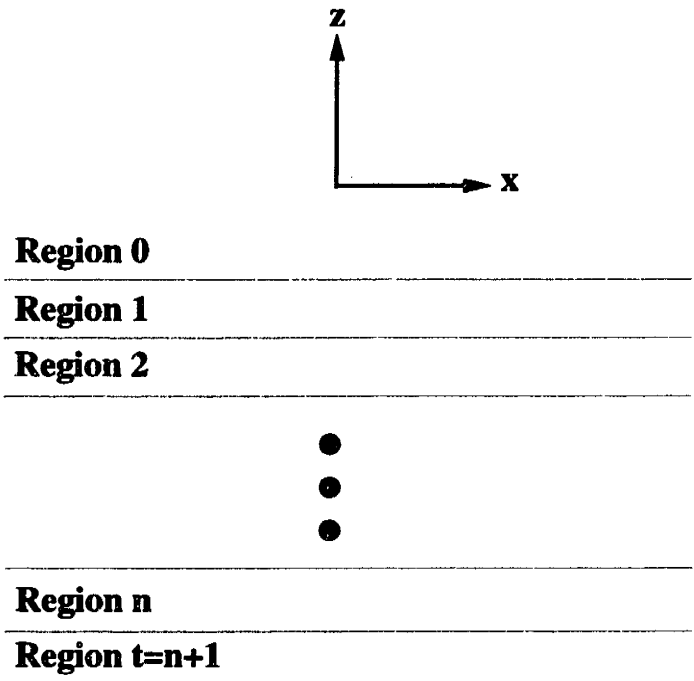
Figure 3-3: A layered medium where the z-axis is normal to all interfaces.

0. Therefore, R_0 is written in the form

$$R_0 = \frac{e^{2ik_z d_0}}{R_{01}} + \cfrac{\left(1 - \frac{1}{R_{01}^2}\right) e^{2i(k_{1z}+k_z)d_0}}{\frac{1}{R_{01}}e^{2ik_{1z}d_0} + \frac{e^{2ik_z d_1}}{R_{12}} + \cfrac{\left(1 - \frac{1}{R_{12}^2}\right) e^{2i(k_{2z}+k_{1z})d_1}}{\frac{1}{R_{12}}e^{2ik_{2z}d_1} + \frac{e^{2ik_{2z}d_2}}{R_{23}} + \cfrac{\cdots}{\ddots \quad \frac{1}{R_{nt}}e^{2ik_{tz}d_n} + R_t}}}$$

$$(3.20)$$

For TM waves, the similar expression as in (3.20) still holds except that $R_{l(l+1)} = \frac{1-p_{l(l+1)}}{1+p_{l(l+1)}}$, and $p_{l(l+1)} = \frac{\epsilon_l k_{(l+1)z}}{\epsilon_{(l+1)} k_{lz}}$.

3.2 Modeling of Frost Flowers

The areal coverage pattern of frost flowers on young sea ice surface does not have a simple geometric feature. Nevertheless, a naturally occurring accumulation process is always expected to be *random*. Although the picture of the actual configuration can be entered into the scattering model, there is no guarantee that merely our macroscopic calculation will be able to account completely for the randomness in the microscopic level. Therefore, the Monte Carlo simulation approach, which is reliable and widely applied in similar situations, is pursued.

The growth process is done only at the macroscopic level. It only specifies the center position of every tiny slush patch. To complete the model for frost flowers, we should also specify the shape of every individual slush unit. Here we choose a rectangular shape as the basic unit, which is indicated in Figure 3-4. The rectangular patch in Figure 3-4 has a few advantages over other geometries in accordance with the computational viewpoint.

It is obvious that, among the various two-dimensional geometric figures, polygons are the easiest to be combined together with one side against another to form a larger
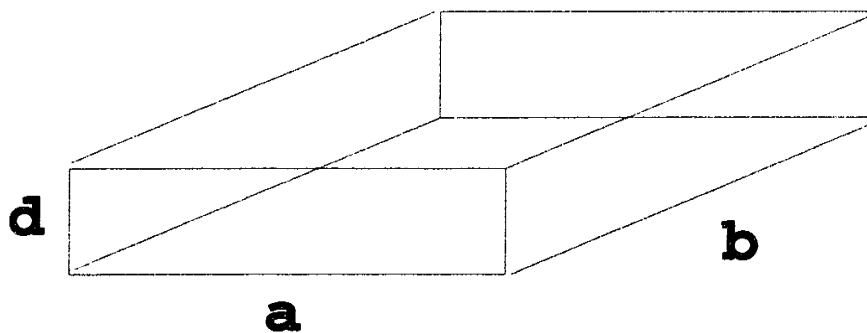
Figure 3-4: The electromagnetic scattering model of frost flowers excluding the flower crystals

fully-connected two-dimensional figure. Among all the polygons, rectangles are most convenient for building blocks. The set of rectangles can be arranged together simply by always keeping every side parallel to another of their sides. Furthermore, we can always construct an arbitrarily irregular area from rectangular building blocks provided that the dimension of each building block is small enough. Thus, rectangular patches are appropriate for later simulation of slush aggregation on sea ice surface. Additionally, we benefit certain flexibility from rectangular building blocks. A slush coverage with a variation of thickness across the ice surface can be simulated with the sufficiently small horizontal dimensions, a and b. In other words, d can depend upon the position where a slush unit is placed. In our case, we use square p atches ($a = b$) so that the generation of slush configurations is even more simplified and the thickness dimension, d, is constant. The latter option is consistent with the reality. As will be evident later, the vertical dimension of a slush unit is much smaller than its horizontal dimension ($d \ll a$) in the specification of simulation parameters. Therefore, the thickness parameter, d, being generalized into a variable with the average $\overline{d} \ll a$ is not expected to make notable differences in terms of backscattering calculations.

3.3   Simulation of Frost Flower Growth

A random walk model is applied in this study to simulate the aggregation process of frost flower formation owing to the fact that the covering pattern of frost flowers is nondeterministic in nature. Since the contribution of frost flower crystals to the C-band radar backscatter is small, only the base area of frost flowers, the slush layer, is considered in this simulation. To imitate the randomness, a total slush layer is thought of as a collection of many small rectangular slush patches. Moreover, the slush layer is assumed to be uniform in thickness at each growth stage because the vertical dimension of frost flower is much smaller than the horizontal dimensions.

32

In the attempt to simulate the CRREL experimental scenarios, we start from the slush unit which is the building block of any simulated slush coverage. From the time-series data of the areal coverage, the dimensions of the corresponding slush unit are designed so that each areal coverage can be accomplished by a number of its slush units. The whole area of sea ice is also divided into blocks depicting the possible placement of the small patches on the area. Consequently, the horizontal dimension of a slush unit must be small enough to discretize the whole area and each areal coverage simultaneously. Thus, the smaller the horizontal dimension of a slush unit is, the more variation of the covering patterns of an areal coverage is. Moreover, it is not crucial that the horizontal dimension of a slush unit is chosen differently for each stage of the frost flower growth since a choice of slush unit dimensions corresponds to a legitimate class of realizations or coverages. However, the vertical dimension is determined according to the measured thicknesses of the slush layer at different stages. Hence, we assume the thickness of the slush layer is uniform and only time-dependent.

With a few initial seed patches, slush patches are grown consecutively around the seeds until the overall areal coverage is reached. The growing process is simulated by a random-walk process. First, a slush patch is initialized randomly from a position. Then, it travels through the two-dimensional space with four possible direction for each step. In every step, the direction is determined randomly. This process is repeated until the walking slush is attached to an "old" slush. In this manner, the growth process of slush patches is simulated. This scheme is illustrated in Figure 3-5.

In this case, a random walk can be initiated from the exterior; nevertheless, the walk is limited inside the area of interest after the walk reaches it to speed up the attachment of a new slush unit. For a fixed coverage, many of such realizations are created to represent a sufficient ensemble of the specific physical picture, which is resolved by the convergent ensemble average of the quantity of interest. In other

words, specifically, the number of realizations has to be large enough to produce the convergent results for backscattering coefficients.

Figure 3-5: The illustrations of the frost flower growth process governed by a series of two-dimensional random walks through the rectangular lattice which spans the area of interest exactly.

Chapter 4

Electromagnetic Model of Sea Ice Covered with Frost Flowers

With the models for the saline ice layer and slush patches described in Chapter 3, an appropriate and computationally feasible scheme for computation of backscattering in presented in this chapter. As discussed in Chapter 2, the backscatter contributions from flower crystals above slush patches and the scattering from brine inclusions and rough interfaces are neglected. Therefore, in developing the scattering model for the frost flowers, we only consider the effect of slush patches. In this scattering model, we first calculate the electromagnetic scattering from a single slush unit first, and then obtain the scattering from the overall slush patch pattern by incorporating the structure factor.

4.1 Coherent Scattering Formulation Based on Volume Integral Equation

In case of the nonuniform slush thickness, the random surface scattering approach can be considered. However, because of the layered medium below the rough surface, the

problem does not satisfy the requirement of the random surface scattering. Since the primary expectation is to obtain an accurate solution to the scattered field in some analytic forms, the extended boundary condition method[37, 3] and the volume integral method[37, 3] are among the viable general approaches. The extended boundary condition method is simple in the scattering problem for virtually any geometry in free space since the free-space dyadic Green's function takes a simple form in some vector field bases. In the situation of an inhomogeneous medium, the surface-integral equation in the extended boundary condition method does not have an simple analytic solution. Similarly, the volume integral equation poses the same difficulty but the single integral equation determines the electric field anywhere completel y. Although there are numerical methods that can lead to a solution in either case, the attempt to find an analytic expression for the scattered field is pursued through the volume integral method as also suggested in [39].

Volume integral equation approach[27] is very useful when studying the scattering problems with inhomogeneous volume scatterers. In the volume integral formulation, the scattered field is related to the internal field of the scattering volume as expected. The formula accounts for the inhomogeneity, $\epsilon_r(\bar{r})$, of the scattering volume by including $k(\bar{r})$, the wavenumber within the inhomogeneity.

Consider a particle with the permittivity $\epsilon_p(\bar{r})$ occupies region V_p,

$$\epsilon(\bar{r}) = \begin{cases} \epsilon_p(\bar{r}) & \bar{r} \in V_p \\ \epsilon_0 & \text{otherwise} \end{cases} \tag{4.1}$$

From Maxwell's curl equations[18]

$$\nabla \times \overline{E} = i\omega\mu_0\overline{H} \tag{4.2}$$

$$\nabla \times \overline{H}(\bar{r}) = -i\omega\epsilon(\bar{r})\overline{E}(\bar{r}) \tag{4.3}$$

37

$\overline{E}$ satisfies the electric field Helmholtz wave equation

$$\nabla \times \nabla \times \overline{E}(\overline{r}) - k_0^2 \epsilon_r(\overline{r})\overline{E}(\overline{r}) = 0 \tag{4.4}$$

where $k_0^2 = \omega^2 \mu_0 \epsilon_0$ and $\epsilon_r(\overline{r}) = \frac{\epsilon_p(\overline{r})}{\epsilon_0}$.

Equation (4.4) can become an inhomogeneous Helmholtz wave equation

$$\nabla \times \nabla \times \overline{E} - k^2\overline{E} = k_0^2(\epsilon_r(\overline{r}) - 1)\overline{E}$$

$$= i\omega\mu_0[-i\omega\epsilon_0(\epsilon_r(\overline{r}) - 1)\overline{E}] \tag{4.5}$$

The right-hand side of (4.5) can be regarded as the equivalent induced current which radiates to give the total electric field solution.

$$\overline{E}(\overline{r}) = \int d\overline{r}'\overline{\overline{G}}(\overline{r},\overline{r}') \cdot i\omega\mu[-i\omega\epsilon(\epsilon_r(\overline{r}') - 1)\overline{E}] + \overline{E}_{inc}(\overline{r}) \tag{4.6}$$

or

$$\overline{E} = \overline{E}_{inc}(\overline{r}) + \int d\overline{r}'(k^2(\overline{r}') - k_0^2)\overline{E}(\overline{r}') \cdot \overline{\overline{G}}(\overline{r},\overline{r}') \tag{4.7}$$

where $\overline{E}_{inc}$ is the incident field which is also the solution to the homogeneous wave equation (4.6), and $\overline{\overline{G}}(\overline{r},\overline{r}')$ is the dyadic Green's function. The dyadic Green's function $\overline{\overline{G}}(\overline{r},\overline{r}')$ can be expressed in terms of scalar Green's function $g(\overline{r},\overline{r}')$.

$$\overline{\overline{G}}(\overline{r},\overline{r}') = \left[\overline{\overline{I}} + \frac{\nabla\nabla}{k_0^2}\right]g(\overline{r},\overline{r}') \tag{4.8}$$

where

$$g(\overline{r},\overline{r}') = \frac{e^{ik_0|\overline{r}-\overline{r}'|}}{4\pi|\overline{r} - \overline{r}'|} \tag{4.9}$$

38

The derivation of (4.8) is given in Appendix A. To solve equations (4.6) and (4.7) , an exact solution for the internal field $\overline{E}(\overline{r}')$ within the integral. This requires to solve Maxwell's equations rigorously based on the given boundary conditions, or other numerical methods such as the Method of Moments[18] in which the unknown internal field is expanded in terms of some basis functions. However, in this study, an approximate solution is sought for the internal field. The approximation is described in the next section.

4.2   Infinite Layer Approximation

Now that the volume integral formulation is used, to obtain the scattered field, the field internal to a slush patch is calculated using the infinite-layer approximation. Since the vertical dimension of a slush layer is much smaller compared to the horizontal expansion over sea ice in the experiment at all observations, the internal field within the slush layer is thus approximated as the field of an infinite dielectric layer model. Physically, the infinite-layer approximation assumes that the slush patch responds to an incident wave as though it is of infinite extent. However, when the slush patch radiates the scattered field, it radiates as a patch of a finite dimension. The reflection coefficients at the interface between sea ice and slush or the interface between sea ice and sea water, can be simply calculated from the effective permittivity of sea ice using the layer model in Chapter 3.

Owing to the fact that the vertical extent of a slush layer is much smaller than the horizontal extent, the object is assumed to span the whole interface between region 0 and region 1. This leads to the problem of layered media which is analytically solvable. However, the resulting internal field is the approximated internal field of a slush unit with finite volume.

For convenience, define the following for the use through the whole context of this
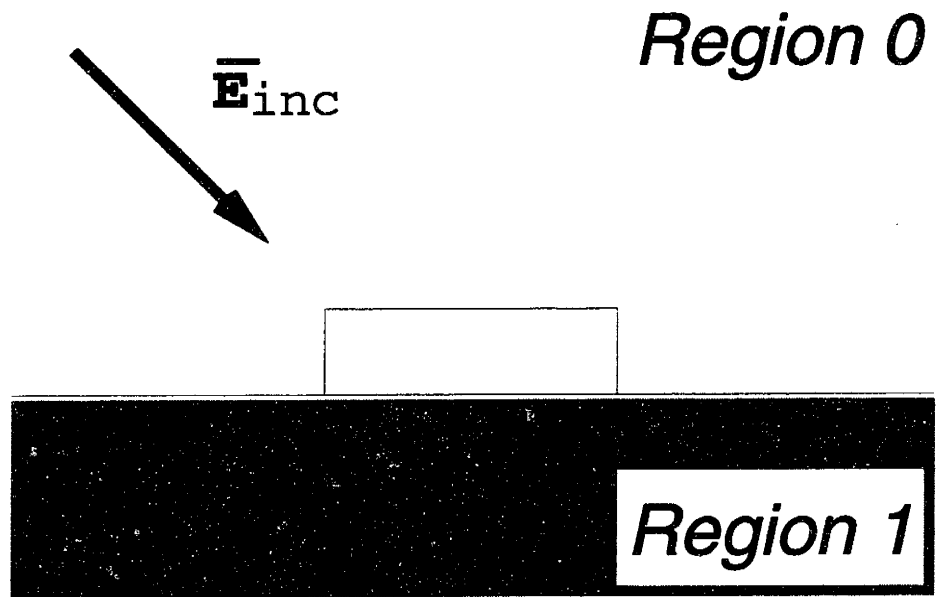
Figure 4-1: The scattering picture of a slush layer in a half space where the lower space is the medium which replaces sea ice

$\overline{E}inc$

Region 0

$z = \dfrac{d}{2}$

Region 2

z

$z = -\dfrac{d}{2}$

Region 1
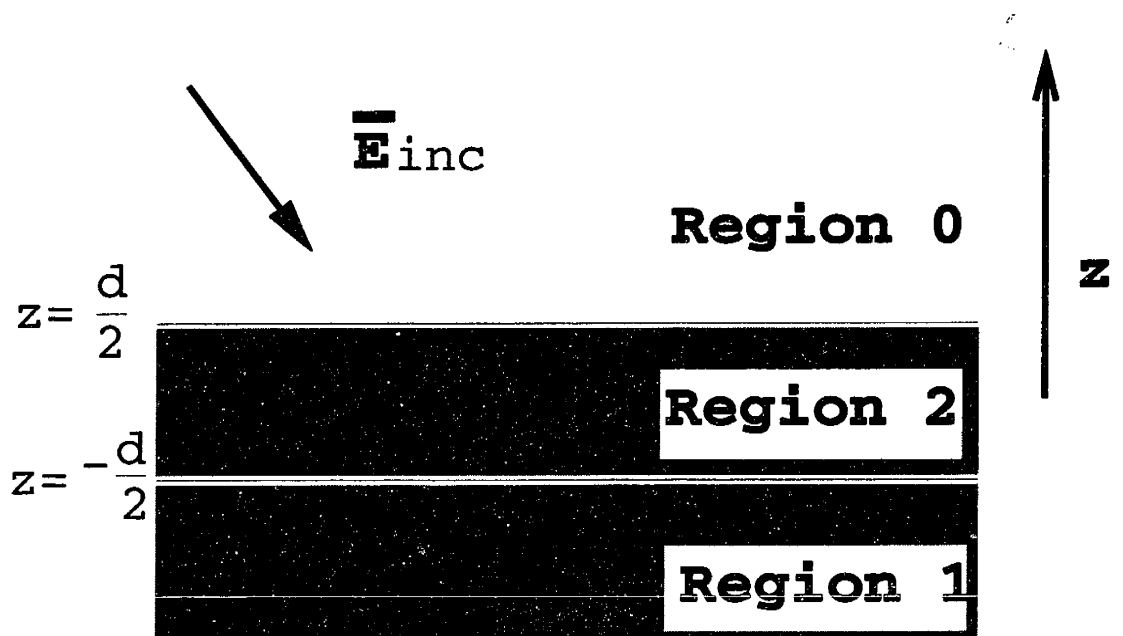
Figure 3

Figure 4-2: The infinite extension of the slush layer in the calculation of the internal field in the slush layer using the infinite-layer approximation

paper. Also, $\overline{k}_i$ is the incident propagation vector. So, for all α,

$$k_{i\alpha z} = \sqrt{k_\alpha^2 - k_{i\perp}^2} \qquad (4.10)$$

$$\overline{k}_{i\alpha} = \overline{k}_{i\perp} + \hat{z}k_{i\alpha z} \qquad (4.11)$$

Given the permittivities and the incident wave, we can solve the two-layer problem as follows[37]. Note, however, that $\epsilon_2 = \epsilon_p$ and 2 and p indices can be used interchangeably and $\overline{k}_0 = \overline{k}_i$. First, we define a orthonormal triplet $(\hat{k}_\alpha^\pm, \hat{h}_\alpha^\pm, \hat{v}_\alpha^\pm)$ for any nonzero propagation vector $\hat{k}_\alpha$, where $\overline{k}_\alpha^\pm = \overline{k}_{\alpha\perp} \pm \hat{z}k_{\alpha z}$.

$$\hat{h}_\alpha^\pm = \frac{\hat{k}_\alpha^\pm \times \hat{z}}{|\hat{k}_\alpha^\pm \times \hat{z}|} \qquad (4.12)$$

$$\hat{v}_\alpha^\pm = \hat{h}_\alpha^\pm \times k_\alpha^\pm \qquad (4.13)$$

Suppose, the fields of the incident wave are

$$\overline{E}_{inc} = (E_{hi}\hat{h}_i + E_{vi}\hat{v}_i)e^{i\overline{k}_i.\overline{r}} \qquad (4.14)$$

$$\overline{H}_{inc} = \frac{1}{\eta}(E_{vi}\hat{h}_i - E_{hi}\hat{v}_i)e^{i\overline{k}_{i\perp}.\overline{r}_\perp + ik_{iz}z} \qquad (4.15)$$

Given the H_{lz} component in the TE case for region l, l=0,1,2, the perpendicular components can be written as

$$\overline{H}_{l\perp}^{TE} = \frac{1}{k_\perp^2}\nabla_\perp\left[\frac{\partial}{\partial z}H_{lz}^{TE}\right] \qquad (4.16)$$

$$\overline{E}_{l\perp}^{TE} = \frac{i\omega\mu}{k_\perp^2}\nabla_\perp \times \overline{H}_{lz}^{TE} \qquad (4.17)$$

Similarly, Given the E_{lz} component in the TM case for region l, l=0,1,2, the perpendicular components can be written as

$$\overline{E}_{l\perp}^{TM} = \frac{1}{k_\perp^2} \nabla_\perp \left[\frac{\partial}{\partial z} E_{lz}^{TM} \right] \tag{4.18}$$

$$\overline{H}_{l\perp}^{TM} = -\frac{i\omega\epsilon_l}{k_\perp^2} \nabla_\perp \times \overline{E}_{lz}^{TM} \tag{4.19}$$

Starting with the TE component of the incident wave, consider the horizontally polarized incidence. Let θ_i and ϕ_i be the angles of the incident propagation vector $\overline{k}_i$. Also, let the origin be at the center of the object. In region 0, i.e. for $z > \frac{d}{2}$

$$H_z = \sqrt{\frac{\epsilon_0}{\mu_0}} E_{hi} \sin\theta_i (e^{ik_{iz}z} + R^{TE}e^{-ik_{iz}z}) e^{i\overline{k}_{i\perp}\cdot\overline{r}_\perp} \tag{4.20}$$

In region 2, i.e. for $-\frac{d}{2} < z < \frac{d}{2}$, we have

$$H_z = \sqrt{\frac{\epsilon_0}{\mu_0}} E_{hi} \sin\theta_i (A_p e^{ik_{i2z}z} + B_p e^{-ik_{i2z}z}) e^{i\overline{k}_{i\perp}\cdot\overline{r}_\perp} \tag{4.21}$$

In region 1, i.e. for $z < -\frac{d}{2}$, we have

$$H_z = \sqrt{\frac{\epsilon_0}{\mu_0}} E_{hi} \sin\theta_i T^{TE} e^{ik_{i1z}z + i\overline{k}_{i\perp}\cdot\overline{r}_\perp} \tag{4.22}$$

Matching the boundary conditions for the continuity of the tangential magnetic induction and the perpendicular magnetic field, we solve for A_p and B_p below, where $R_{\alpha\beta}^{TE} = \frac{k_{i\alpha z} - k_{i\beta z}}{k_{i\alpha z} + k_{i\beta z}}$.

$$R^{TE} e^{-ik_{iz}d} = \frac{R_{02}^{TE} - R_{12}^{TE} e^{-2ik_{i2z}d}}{1 - R_{02}^{TE} R_{12}^{TE}} \tag{4.23}$$

43

$$A_p e^{ik_{2z}\frac{d}{2}} = \frac{1}{2}\left\{(1 + \frac{k_{iz}}{k_{2z}})e^{ik_{iz}\frac{d}{2}} + R^{TE}(1 - \frac{k_{iz}}{k_{2z}})e^{-ik_{iz}\frac{d}{2}}\right\} \qquad (4.24)$$

$$B_p e^{-ik_{2z}\frac{d}{2}} = \frac{1}{2}\left\{(1 - \frac{k_{iz}}{k_{2z}})e^{ik_{iz}\frac{d}{2}} + R^{TE}(1 + \frac{k_{\cdot}}{k_{2z}})e^{-ik_{iz}\frac{d}{2}}\right\} \qquad (4.25)$$

Apply the similar procedure for the TM case. In region 0,

$$E_z = -E_{vi}\sin\theta_i(e^{ik_{iz}z} + R^{TM}e^{-ik_{iz}z})e^{i\overline{k}_{i\perp}\cdot\overline{r}_\perp} \qquad (4.26)$$

In region 2, i.e. for $-\frac{d}{2} < z < \frac{d}{2}$, we have

$$E_z = -E_{vi}\sin\theta_i(C_p e^{ik_{i2z}z} + D_p e^{-ik_{i2z}z})e^{i\overline{k}_{i\perp}\cdot\overline{r}_\perp} \qquad (4.27)$$

In region 1, i.e. for $z < -\frac{d}{2}$, we have

$$E_z = -E_{vi}\sin\theta_i T^{TM}e^{ik_{i1z}z + i\overline{k}_{i\perp}\cdot\overline{r}_\perp} \qquad (4.28)$$

Matching the boundary conditions for the continuity of the tangential electric field and the electric flux density, we solve for C_p and D_p below, where $R^{TM}_{\alpha\beta} = \frac{\epsilon_\beta k_{i\alpha z} - \epsilon_\alpha k_{i\beta z}}{\epsilon_\beta k_{i\alpha z} + \epsilon_\alpha k_{i\beta z}}$.

$$R^{TM}e^{-ik_{iz}d} = \frac{R^{TM}_{02} - R^{TM}_{12}e^{-2ik_{2z}d}}{1 - R^{TM}_{02}R^{TM}_{12}} \qquad (4.29)$$

$$C_p e^{ik_{2z}\frac{d}{2}} = \frac{1}{2}\left\{(\frac{\epsilon_0}{\epsilon_2} + \frac{k_{iz}}{k_{2z}})e^{ik_{iz}\frac{d}{2}} + R^{TM}(\frac{\epsilon_0}{\epsilon_2} - \frac{k_{iz}}{k_{2z}})e^{-ik_{iz}\frac{d}{2}}\right\} \qquad (4.30)$$

$$D_p e^{-ik_{2z}\frac{d}{2}} = \frac{1}{2}\left\{(\frac{\epsilon_0}{\epsilon_2} - \frac{k_{iz}}{k_{2z}})e^{ik_{iz}\frac{d}{2}} + R^{TM}(\frac{\epsilon_0}{\epsilon_2} + \frac{k_{iz}}{k_{2z}})e^{-ik_{iz}\frac{d}{2}}\right\} \qquad (4.31)$$

Finally, we can represent the incident field as the sum of TE and TM components:

$$\overline{E}_{inc} = [\hat{h}(\overline{k}_i)\hat{h}(\overline{k}_i) + \hat{v}(\overline{k}_i)\hat{v}(\overline{k}_i)]e^{i\overline{k}_i.\overline{r}} \cdot \overline{E}_{i0} \qquad (4.32)$$

Then, from (4.21) , (4.27) , and (4.32) , we can obtain the internal field in region 2:

$$\overline{E}_{int} \approx \left[\left(A_p\hat{h}(\overline{k}_{i1}^-)\hat{h}(\overline{k}_i) + \frac{k_i}{k_2}C_p\hat{h}(\overline{k}_{i1}^-)\hat{h}(\overline{k}_i) \right) e^{i\overline{k}_{1i}^-.\overline{r}} + \right.$$

$$\left. \left(B_p\hat{h}(\overline{k}_{1i}^+)\hat{h}(\overline{k}_i) + \frac{k_i}{k_2}D_p\hat{h}(\overline{k}_{i1}^+)\hat{h}(\overline{k}_i) \right) e^{i\overline{k}_{i1}^+.\overline{r}} \right] \cdot \overline{E}_{i0} \qquad (4.33)$$

where A_p, B_p, C_p, and D_p are defined in (4.24) , (4.25) , (4.30) , and (4.31) .

4.3   Spectral Expansion of the Half-Space dyadic Green's function

A half-space Green's function is used for the volume integral formulation to include the interaction with the interface between the air and the sea ice. The reflection coefficient at the interface between air and sea ice is calculated by using the layer model for sea ice as previously mentioned and the recursive formula for the reflection coefficient at each layer. Therefore, we have two equations for the half-space dyadic Green's function.

$$\nabla \times \nabla \times \overline{\overline{G}}(\overline{r},\overline{r}') - k_0^2\overline{\overline{G}}(\overline{r},\overline{r}') = \overline{\overline{I}}\delta(\overline{r} - \overline{r}') \qquad (4.34)$$

when $\overline{r}$ is in region 0.

$$\nabla \times \nabla \times \overline{\overline{G}}(\overline{r},\overline{r}') - k_1^2\overline{\overline{G}}(\overline{r},\overline{r}') = \overline{\overline{I}}\delta(\overline{r} - \overline{r}') \qquad (4.35)$$

where $\overline{r}$ is in region 1.

Although each value of wavenumbers is associated with a free-space dyadic Green's function[1], $\overline{\overline{G}}_i(\overline{r}, \overline{r}') = \left[\overline{\overline{I}} + \frac{1}{k^2}\nabla\nabla\right]\frac{e^{ik_i|\overline{r}-\overline{r}'|}}{4\pi|\overline{r}-\overline{r}'|}$, the boundary conditions for (4.35) and (4.34) below are not satisfied using those dyads.

$$\hat{z} \cdot \overline{\overline{G}}(\overline{r}_0, \overline{r}') = \hat{z} \cdot \overline{\overline{G}}(\overline{r}_1, \overline{r}') \tag{4.36}$$

$$\hat{z} \times \overline{\overline{G}}(\overline{r}_0, \overline{r}') = \hat{z} \times \overline{\overline{G}}(\overline{r}_1, \overline{r}') \tag{4.37}$$

where $\overline{r}_0$ and $\overline{r}_1$ indicate that the dyadic is defined in region 0 and 1 respectively.

Then, we might need to solve the equations (4.35) and (4.34) directly in the frequency domain. Since we have already solved the free-space case, some insights into the solution of the half-space case are expected to be obtained from the free-space solution. Owing to the fact that the $\overline{r}$-space solution is irrelevant as previously mentioned, we eventually focus on the the $\overline{k}$-space solution or the spectral expansion of the free-space dyadic Green's function.

$$\overline{\overline{G}}(\overline{r}, \overline{r}') = -\hat{z}\hat{z}\delta(\overline{r} - \overline{r}') - \frac{i}{8\pi^2}\int\int_{-\infty}^{\infty} dk_x dk_y \frac{1}{k_{0z}}$$
$$\left\{ [\hat{h}_0^{\pm} e^{i\overline{k}_0^{\pm}\cdot\overline{r}}][\hat{h}_0^{\pm} e^{-i\overline{k}_0^{\pm}\cdot\overline{r}'}] + [\hat{v}_0^{\pm} e^{i\overline{k}_0^{\pm}\cdot\overline{r}}][\hat{v}_0^{\pm} e^{-i\overline{k}_0^{\pm}\cdot\overline{r}'}] \right\} \tag{4.38}$$

for $\pm(z - z') > 0$.

With the spectral expansion, we view the operation of the dyadic Green's function on a frequency component of a vector field by simply looking at the spectrum of the dyadic Green's function itself. Thus, we consider the integrand in (4.38) for more details. From the understanding of the details which are packed into the expression for the free-space dyadic Green's function, we hope for a systematic deduction towards the case of a layered medium.

---

[1]See appendix A

46

For $z > z'$, the observation point is forward in the z-direction; therefore, the free-space dyadic Green's function propagates waves which has the positive k_z from $\bar{r}'$, the "source" point, to $\bar{r}$, the "observation" point. Therefore, the dyadic Green's function has two terms for $\hat{e}$- and $\hat{h}$-polarizations or TE and TM polarizations respectively. The case of $z < z'$ can be thought of in the similar fashion. The only index 0 shows that the propagation takes place in the only medium indexed 0.

For a layered medium, we employ $\overline{\overline{G}}_{\alpha\beta}(\bar{r}, \bar{r}')$ as the dyadic Green's function for $\bar{r}$ in region α and $\bar{r}'$ in region β. For the half-space case as Figure 4-3, the indices take values of 0 and 1.

In our case, we are only interested in $\overline{\overline{G}}_{00}(\bar{r}, \bar{r}')$ since the field point and transmitter are located in region 0. We can then make a similar argument about terms in the spectral expansion to that argument we have made about the free-space dyadic Green's function. Nevertheless, a rigorous derivation of the half-space dyadic Green's function is given in Appendix B.

For $z > z'$, the half-space dyadic Green's function $\overline{\overline{G}}_{00}(\bar{r}, \bar{r}')$ contains a direct propagation and a reflected propagation. The former is represented by the same expressions as in the free-space dyadic Green's function. The latter corresponds to a downward free-space propagation from the point $\bar{r}'$ to the interface, the reflection at the interface, and a upward free-space propagation from the surface to the point $\bar{r}$.

For $z < z'$, we only expect the change in the direct propagation terms since the reflected propagation, as an interaction with the interface, only depends on z and z', not their relation. The direct propagation integrand merely follows the free-space case. Hence, the half-space Green's function $\overline{\overline{G}}_{00}(\bar{r}, \bar{r}')$ for $\pm(z - z') \geq 0$ and $\bar{r}, \bar{r}' \epsilon V_0$ is expressed as
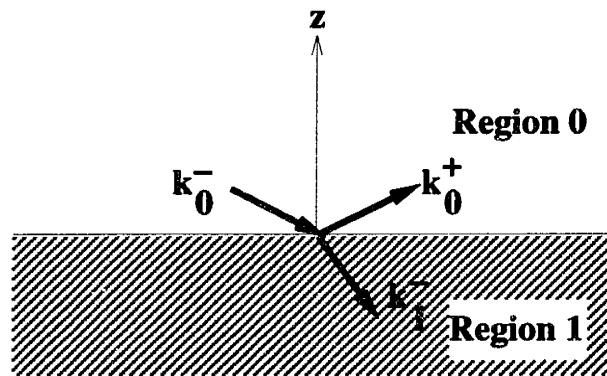
Figure 4-3: The picture of a half-space medium with the incidence in region 0

$$\overline{\overline{G}}_{00}(\overline{r}, \overline{r}') = -\hat{z}\hat{z}\delta(\overline{r} - \overline{r}') + \frac{i}{8\pi^2} \int_{-\infty}^{\infty} \int_{-\infty}^{\infty} \frac{dk_x dk_y}{k_{0z}} \left\{ \{\hat{h}_0^{\pm} e^{i\overline{k_0^{\pm}}.\overline{r}}\}\{\hat{h}_0^{\pm} e^{-i\overline{k_0^{\pm}}.\overline{r}'}\} \right.$$

$$+ \{\hat{v}_0^{\pm} e^{i\overline{k_0^{\pm}}.\overline{r}}\}\{\hat{v}_0^{\pm} e^{-i\overline{k_0^{\pm}}.\overline{r}'}\} + R^{TE}(k_x, k_y, k_{0z})\{\hat{h}_0^{+} e^{i\overline{k_0^{+}}.\overline{r}}\}\{\hat{h}_0^{-} e^{-i\overline{k_0^{-}}.\overline{r}'}\}$$

$$\left. + R^{TM}(k_x, k_y, k_{0z})\{\hat{v}_0^{+} e^{i\overline{k_0^{+}}.\overline{r}}\}\{\hat{v}_0^{-} e^{-i\overline{k_0^{-}}.\overline{r}'}\} \right\} \qquad (4.39)$$

for $\pm(z - z') \geq 0$, where the reflection coefficients R^{TE} and R^{TM} are calculated by considering the effective reflection at the top surface of the ice. With the layer model, the reflection coefficients are given in Chapter 3 as R_0.

4.4 Scattered Electric Field

We substitute the spectral expansion of the half-space dyadic Green's function into the expression for the scattered field from the model. Then, we obtain

$$\overline{E}_S = \frac{k^2}{8\pi^2} \int d\overline{r}' (\frac{\epsilon_1}{\epsilon_0} - 1) \int_{-\infty}^{\infty} \int_{-\infty}^{\infty} \frac{dk_x dk_y}{k_{0z}} \left\{ \{\hat{h}_0^{\pm} e^{i\overline{k_0^{\pm}}.\overline{r}}\}\{\hat{h}_0^{\pm} e^{-i\overline{k_0^{\pm}}.\overline{r}'}\} \right.$$

$$+ \{\hat{v}_0^{\pm} e^{i\overline{k_0^{\pm}}.\overline{r}}\}\{\hat{v}_0^{\pm} e^{-i\overline{k_0^{\pm}}.\overline{r}'}\} + R^{TE}(k_x, k_y, k_{0z})\{\hat{h}_0^{+} e^{i\overline{k_0^{+}}.\overline{r}}\}\{\hat{h}_0^{-} e^{-i\overline{k_0^{-}}.\overline{r}'}\}$$

$$\left. + R^{TM}(k_x, k_y, k_{0z})\{\hat{v}_0^{+} e^{i\overline{k_0^{+}}.\overline{r}}\}\{\hat{v}_0^{-} e^{-i\overline{k_0^{-}}.\overline{r}'}\} \right\} \cdot \overline{E}_{int}(\overline{r}') \qquad (4.40)$$

where the internal field, $\overline{E}_{int}(\overline{r}')$, is estimated by the infinite layer approximation as

$$\overline{E}_{int}(\overline{r}') \approx \left[(A\hat{h}(\overline{k_1^{-}})\hat{h}(\overline{k_0^{-}}) + \frac{k_0}{k_1}C\hat{v}(\overline{k_1^{-}})\hat{v}(\overline{k_0^{-}}))e^{i\overline{k_1^{-}}.\overline{r}'} \right.$$

$$\left. + (B\hat{h}(\overline{k_1^{+}})\hat{h}(\overline{k_0^{-}}) + \frac{k_0}{k_1}D\hat{v}(\overline{k_1^{+}})\hat{v}(\overline{k_0^{-}}))e^{i\overline{k_1^{+}}.\overline{r}'} \right] \qquad (4.41)$$

where A, B, C and D are obtained from A_p, B_p, C_p and D_p as defined in (4.24) , (4.25) , (4.30) and (4.31) by replacing ϵ_2 with ϵ_1 and ϵ_1 with ϵ_0.

By observation, the five-fold integral of the total field in the spectral form in (4.41) does not have a simple form. However, the volume integral corresponding to the rectangular shape of each slush unit of the slush layer can be simplied into a double integral of the spectrum by performing the volume integral analytically. We can rewrite $\overline{E}_s$ as the sum of volume integrals with domains V_1, V_2, ..., which correspond to slush units 1, 2, ... :

$$\overline{E}_S = \frac{ik_0^2}{8\pi^2}(\frac{\epsilon_1}{\epsilon_0} - 1)\sum_{i=1}^{n}\int_{V_i}d\bar{r}'\int_{-\infty}^{\infty}\int_{-\infty}^{\infty}\frac{dk_xdk_y}{k_{0z}}\left\{\hat{h}_0^{\pm}e^{i\overline{k_0^{\pm}}.\bar{r}}\right\}\{\hat{h}_0^{\pm}e^{-i\overline{k_0^{\pm}}.\bar{r}'}\}+$$

$$\{\hat{v}_0^{\pm}e^{i\overline{k_0^{\pm}}.\bar{r}}\}\{\hat{v}_0^{\pm}e^{-i\overline{k_0^{\pm}}.\bar{r}'}\} + R^{TE}(k_x, k_y, k_{0z})\{\hat{h}_0^+e^{i\overline{k_0^+}.\bar{r}}\}\{\hat{h}_0^-e^{-i\overline{k_0^-}.\bar{r}'}\}+$$

$$R^{TM}(k_x, k_y, k_{0z})\{\hat{v}_0^+e^{i\overline{k_0^+}.\bar{r}}\}\{\hat{v}_0^-e^{-i\overline{k_0^-}.\bar{r}'}\}\} \cdot \left[\left(A\hat{h}(\overline{k_{i1}^-})\hat{h}(\overline{k_i}) + \frac{k_i}{k_1}C\hat{v}(\overline{k_{i1}^-})\hat{v}(\overline{k_i})\right)e^{i\overline{k_{i1}^-}.\bar{r}'}\right.$$

$$\left. + \left(B\hat{h}(\overline{k_{1i}^+})\hat{h}(\overline{k_i}) + \frac{k_i}{k_1}D\hat{v}(\overline{k_{i1}^+})\hat{v}(\overline{k_i})\right)e^{i\overline{k_{i1}^+}.\bar{r}'}\right] \cdot \overline{E}_{i0} \qquad (4.42)$$

By performing the integral over $\bar{r}'$ directly, we can obtain the analytic representation of $\overline{E}_s$ in terms of a double integral over $\overline{k}$-space. Note that $\bar{r}_m$ is the center position of the m-th slush unit.

$$\overline{E}_S = \frac{ik_0^2}{8\pi^2}(\frac{\epsilon_1}{\epsilon_0} - 1)\sum_{m=1}^{N}\int_{-\infty}^{\infty}\int_{-\infty}^{\infty}\frac{dk_xdk_y}{k_{0z}}e^{i\overline{k_0^+}.\bar{r}}\frac{\sin((k_x - k_{ix})a)}{(k_x - k_{ix})a}\frac{\sin((k_y - k_{iy})b)}{(k_y - k_{iy})b}\Bigg\{$$

$$\hat{e}_0^+\hat{e}_0^+.\hat{e}(\overline{k_{i1}^-})\hat{e}(\overline{k_i})Ae^{i(\overline{k_{i1}^-}-\overline{k_0^+}).\bar{r}_m}F^{(+-)} + \hat{e}_0^+\hat{e}_0^+.\hat{v}(\overline{k_{i1}^-})\hat{v}(\overline{k_i})Be^{i(\overline{k_{i1}^-}-\overline{k_0^+}).\bar{r}_m}F^{(+-)}$$

$$+\hat{v}_0^+\hat{v}_0^+.\hat{e}(\overline{k_{i1}^-})\hat{e}(\overline{k_i})Ae^{i(\overline{k_{i1}^-}-\overline{k_0^+}).\bar{r}_m}F^{(+-)} + \hat{v}_0^+\hat{v}_0^+.\hat{v}(\overline{k_{i1}^-})\hat{v}(\overline{k_i})Be^{i(\overline{k_{i1}^-}-\overline{k_0^+}).\bar{r}_m}F^{(+-)}$$

$$+R_{0p}^{TE}(k_x, k_y, k_{0z})\hat{e}_0^+\hat{e}_0^-.\hat{e}(\overline{k_{i1}^-})\hat{e}(\overline{k_i})Ae^{i(\overline{k_{i1}^-}-\overline{k_0^+}).\bar{r}_m}F^{(--)}$$

$$+R_{0p}^{TE}(k_x, k_y, k_{0z})\hat{e}_0^+\hat{e}_0^-.\hat{v}(\overline{k_{i1}^-})\hat{v}(\overline{k_i})Be^{i(\overline{k_{i1}^-}-\overline{k_0^+}).\bar{r}_m}F^{(--)}$$

$$+ R_{0p}^{TM}(k_x, k_y, k_{0z}) \hat{v}_0^+ \hat{v}_0^- . \hat{e}(\overline{k}_{i1}^-) \hat{e}(\overline{k}_i) A e^{i(\overline{k}_{i1}^- - \overline{k}_0^+).\vec{r}_m} F^{(--)}$$

$$+ R_{0p}^{TM}(k_x, k_y, k_{0z}) \hat{v}_0^+ \hat{v}_0^- . \hat{v}(\overline{k}_{i1}^-) \hat{v}(\overline{k}_i) B e^{i(\overline{k}_{i1}^- - \overline{k}_0^+).\vec{r}_m} F^{(--)}$$

$$+ \hat{e}_0^+ \hat{e}_0^+ . \hat{e}(\overline{k}_{i1}^+) \hat{e}(\overline{k}_i) \frac{k_i}{k_1} C e^{i(\overline{k}_{i1}^+ - \overline{k}_0^+).\vec{r}_m} F^{(++)} + \hat{e}_0^+ \hat{e}_0^+ . \hat{v}(\overline{k}_{i1}^-) \hat{v}(\overline{k}_i) \frac{k_i}{k_1} D e^{i(\overline{k}_{i1}^+ - \overline{k}_0^+).\vec{r}_m} F^{(++)}$$

$$+ \hat{v}_0^+ \hat{v}_0^+ . \hat{e}(\overline{k}_{i1}^+) \hat{e}(\overline{k}_i) \frac{k_i}{k_1} C e^{i(\overline{k}_{i1}^+ - \overline{k}_0^+).\vec{r}_m} F^{(++)} + \hat{v}_0^+ \hat{v}_0^+ . \hat{v}(\overline{k}_{i1}^+) \hat{v}(\overline{k}_i) \frac{k_i}{k_1} D e^{i(\overline{k}_{i1}^+ - \overline{k}_0^+).\vec{r}_m} F^{(++)}$$

$$+ R_{0p}^{TE}(k_x, k_y, k_{0z}) \hat{e}_0^+ \hat{e}_0^- . \hat{e}(\overline{k}_{i1}^+) \hat{e}(\overline{k}_i) \frac{k_i}{k_1} C e^{i(\overline{k}_{i1}^+ - \overline{k}_0^+).\vec{r}_m} F^{(-+)}$$

$$+ R_{0p}^{TE}(k_x, k_y, k_{0z}) \hat{e}_0^+ \hat{e}_0^- . \hat{v}(\overline{k}_{i1}^+) \hat{v}(\overline{k}_i) \frac{k_i}{k_1} D e^{i(\overline{k}_{i1}^+ - \overline{k}_0^+).\vec{r}_m} F^{(-+)}$$

$$+ R_{0p}^{TM}(k_x, k_y, k_{0z}) \hat{v}_0^+ \hat{v}_0^- . \hat{e}(\overline{k}_{i1}^+) \hat{e}(\overline{k}_i) \frac{k_i}{k_1} C e^{i(\overline{k}_{i1}^+ - \overline{k}_0^+).\vec{r}_m} F^{(-+)}$$

$$\left. + R_{0p}^{TM}(k_x, k_y, k_{0z}) \hat{v}_0^+ \hat{v}_0^- . \hat{v}(\overline{k}_{i1}^+) \hat{v}(\overline{k}_i) \frac{k_i}{k_1} D e^{i(\overline{k}_{i1}^+ - \overline{k}_0^+).\vec{r}_m} F^{(-+)} \right\} . \overline{E}_{i0} \qquad (4.43)$$

where

$$F^{(\pm\pm)} = \frac{\sin((\pm k_{0z} \pm k_{i1z})d)}{(\pm k_{0z} \pm k_{i1z})d} \qquad (4.44)$$

This evaluation certainly reduce a great deal of computational complexity in general. Nevertheless, the final result still requires double integrals over $\overline{k}$-space for all the slush units, so the computation is still very intensive. Fortunately, the scattered field we need to calculate is in the far-field region. As we can see in the following section, in the far-field region, the scattered field from over all slush patches V_1, V_2, ... can be approximated as the scattered field from a single patch times a structure factor related to the center position of V_1, V_2, ... This approximation could reduce a lot of computational complexity.

To calculate the scattered field from one slush patch, we still need to carry out the numerical integration over the $\overline{k}$-space. Again, on the basis of the far-field assumption, we can use stationary-phase method to get an approximated analytic result.

51

4.4.1 Method of Stationary Phase

The method as explained in [4] addresses the key features of the *stationary phase integral*. First of all, the exponent of the exponetial function in the integrand is *nonlinear in the integration variables and oscillates rapidly*; in contrast, the other factors in the integrand vary slowly. We intend to verify later that the surface integral concerning the bistatic scattering coefficients is a stationary phase integral. Hence, this method can be applied efficiently to the expression of our interest.

We intend to express a general stationary phase integral in the form that fits our specific purpose. Therefore, let's express a stationary phase integral in the form

$$\Gamma(\hat{r}) = \int \int dk_x dk_y \Psi(k_x, k_y) e^{i\phi(k_x, k_y)} \tag{4.45}$$

where $\phi(k_x, k_y) = \overline{k} \cdot \overline{r}' = k_x x' + k_y y' + k_z(k_x, k_y) z'$.

Clearly, note that, given a function ϕ, there is a unique function, k_z, which only differs by the bilinear function, $f(k_x, k_y) = k_x x' + k_y y'$. According to the notion of stationary phase integrals, Ψ is slowly varying and ϕ is nonlinear. Hence, k_z is also nonlinear. It is quite clear, therefore, that the integral associated to the scattered field has fallen into this category so far since $k_z = \sqrt{k^2 - k_x^2 - k_y^2}$ for a wavenumber k.

We pay attention to the point on the surface of integration where the phase function is almost stationary in all directions in some of its neighborhoods. If such point exists, the phases of waves emanating from the neighborhood of the so-called *stationary point* of the phase function are nearly in phase with each other, so the waves interfere constructively in propagating toward an observer in the far zone. On the other hand, those phases outside the neighborhood, however, are out of phase, so the waves interfere destructively toward the same observer. As a result, to the observer in the far zone, the scattered wave appears as though it comes from only

a small neighborhood of the stationary point of the phase function, the stationary phase point.

The derivatives of the phase function ϕ can be easily computed. At the stationary phase point (k_{xS}, k_{yS}), $\frac{\partial}{\partial k_x}\phi = 0$ and $\frac{\partial}{\partial k_y}\phi = 0$. That is, k_{xS} and k_{yS} are the solution of the system of equations

$$x' + z'\frac{\partial}{\partial k_x}k_z(k_{xS}, k_{yS}) = 0 \qquad (4.46)$$

$$y' + z'\frac{\partial}{\partial k_y}k_z(k_{xS}, k_{yS}) = 0 \qquad (4.47)$$

Let $Q(k_x, k_y)$ be the second-order expansion of ϕ around the stationary phase point (k_{xS}, k_{yS}). Therefore, Q takes the form

$$Q(k_x, k_y) = \alpha k_x^2 + \beta k_x k_y + \gamma k_y^2 \qquad (4.48)$$

By approximating the phase function up to the second order corresponding to Q in (4.48), the stationary phase integral (4.45) is now approximated by

$$\Gamma(\hat{r}) = \Psi(k_{xS}, k_{yS})e^{-i\phi(k_{xS},k_{yS})} \int\int dk_x dk_y e^{iQ(k_x,k_y)} \qquad (4.49)$$

Note that all first-order derivatives are identically zero at a stationary phase point. This is the stationary phase approximation to the stationary phase integral (4.44). The resulting double Gaussian integral can be carried out analytically. Moreover, by some linear transformations in the integration variables, the integral can be simplified into the product of two Gaussian integrals.

The stationary phase approximation reads that the component of the waves at the stationary phase point contributes the most in the process represented by the integration provided that the phase differences among the wave components are much

greater that the amplitude differences among them. Accordingly, the approximated expression takes the amplitudes at the stationary phase point as the representative of the whole spectrum since the constructive interference is only located around the stationary phase point. Therefore, the wave component at the stationary phase point dominates through the process. The fact that the amplitude distribution is *relatively stationary* supports the extraction of the amplitude term evaluated at the stationary phase point outside the integral. Furthermore, in certain situations, we expect further and more specific physical interpretation of the method of stationary phase.

4.4.2   Far-Field Approximation of the Half-Space dyadic Green's function

Starting from the half-space dyadic Green's function,

$$\overline{\overline{G}}_{00}(\overline{r}, \overline{r}') = -\hat{z}\hat{z}\delta(\overline{r} - \overline{r}') + \frac{i}{8\pi^2} \int_{-\infty}^{\infty} \int_{-\infty}^{\infty} \frac{dk_x dk_y}{k_{0z}} \left\{ \{\hat{h}_0^{\pm} e^{i\overline{k_0^{\pm}} \cdot \overline{r}}\}\{\hat{h}_0^{\pm} e^{-i\overline{k_0^{\pm}} \cdot \overline{r}'}\} \right.$$

$$+ \{\hat{v}_0^{\pm} e^{i\overline{k_0^{\pm}} \cdot \overline{r}}\}\{\hat{v}_0^{\pm} e^{-i\overline{k_0^{\pm}} \cdot \overline{r}'}\} + R^{TE}(k_x, k_y, k_{0z})\{\hat{h}_0^{+} e^{i\overline{k_0^{+}} \cdot \overline{r}}\}\{\hat{h}_0^{-} e^{-i\overline{k_0^{-}} \cdot \overline{r}'}\}$$

$$\left. + R^{TE}(k_x, k_y, k_{0z})\{\hat{v}_0^{+} e^{i\overline{k_0^{+}} \cdot \overline{r}}\}\{\hat{v}_0^{-} e^{-i\overline{k_0^{-}} \cdot \overline{r}'}\} \right\} \tag{4.50}$$

for $\pm(z - z') \geq 0$.

We have a particular interest in the far-field range corresponding to the regime $z > z'$. Then, for $z > z'$, we rearrange (4.50) into

$$\overline{\overline{G}}_{00}(\overline{r}, \overline{r}') = \frac{i}{8\pi^2} \int_{-\infty}^{\infty} \int_{-\infty}^{\infty} \frac{dk_x dk_y}{k_{0z}} \left\{ [\hat{h}_0^{+} \hat{h}_0^{+}] \right.$$

$$+ [\hat{v}_0^{+} \hat{v}_0^{+}] + R^{TE}(k_x, k_y, k_{0z}) e^{i(-\overline{k_0^{-}} + \overline{k_0^{+}}) \cdot \overline{r}'} [\hat{h}_0^{+} \hat{h}_0^{-}]$$

54

$$+R^{TM}(k_x, k_y, k_{0z})e^{i(-\overline{k_0}+\overline{k_0^+}).\vec{r}'}[\hat{v}_0^+ \hat{v}_0^-]\Big\} e^{-i\overline{k_0^+}.\vec{r}'}e^{i\overline{k_0^+}.\vec{r}} \qquad (4.51)$$

We want to calculate an approximated expression for (4.51) by applying the stationary phase method on the integral part. Accordingly, the phase associated to the integrand is

$$\phi(k_x, k_y) = \overline{k_0^+}.\vec{r}$$

Thus, we have, at the stationary point,

$$\frac{k_x}{x} = \frac{k_{0z}}{z} \qquad (4.52)$$

$$\frac{k_y}{y} = \frac{k_{0z}}{z} \qquad (4.53)$$

The stationary point is, therefore, $(k_0\frac{x}{r}, k_0\frac{y}{r})$. At the point, we have

$$k_0^+ = k_0\hat{r} \qquad (4.54)$$

Besides the notation we have employed for $\hat{h}$ and $\hat{v}$, the additional notation below displays the functional definition of the basis elements more clearly. The two notations will be used interchangeably for convenience.

$$\hat{h}(\overline{k}) = \frac{\overline{k} \times \hat{z}}{|\overline{k} \times \hat{z}|} = \hat{h}(\hat{k})$$

$$\hat{v}(\overline{k}) = \frac{\hat{h}(\overline{k}) \times \overline{k}}{|\hat{h}(\overline{k}) \times \overline{k}|} = \hat{h}(\hat{k}) \times \hat{k}$$

To relate to the old notation, we obtain

$$\hat{h}_n^\pm = \hat{h}(\overline{k}_n^\pm) = \hat{h}(\hat{k}_n^\pm)$$

55

$$\hat{v}_n^{\pm} = \hat{v}(\overline{k}_n^{\pm}) = \hat{v}(\hat{k}_n^{\pm})$$

where n is an index of layers in a z-layered medium.

To construct the quadratic form of the phase function, the second-order partial derivatives of the phase function are calculated:

$$\frac{\partial^2}{\partial k_x^2} \Phi(k_x, k_y) = -z \left(\frac{1}{k_{0z}} + \frac{k_x^2}{k_{0z}^3} \right)$$

$$\frac{\partial^2}{\partial k_y^2} \Phi(k_x, k_y) = -z \left(\frac{1}{k_{0z}} + \frac{k_y^2}{k_{0z}^3} \right)$$

$$\frac{\partial^2}{\partial k_x \partial k_y} \Phi(k_x, k_y) = z \frac{k_x k_y}{k_{0z}^3}$$

Then, from stationary-phase approximation, the dyadic Green's function is

$$\overline{\overline{G}}_{00}(\overline{r}, \overline{r}') = \left\{ [\hat{h}(\hat{r})\hat{h}(\hat{r})] + [\hat{v}(\hat{r})\hat{v}(\hat{r})] \right.$$

$$\left. + R^{TE}(k_0\hat{r})e^{ik_0(-\hat{r}^- + \hat{r}) \cdot \overline{r}'}[\hat{h}(\hat{r})\hat{h}(\hat{r}^-)] + R^{TM}(k_0\hat{r})e^{ik_0(-\hat{r}^- + \hat{r}) \cdot \overline{r}'}[\hat{v}(\hat{r})\hat{v}(\hat{r}^-)] \right\} e^{-ik_0\hat{r} \cdot \overline{r}'} I(\overline{r}) \tag{4.55}$$

where $\hat{r}^- = \hat{r} - 2(\hat{r})_z \hat{z}$ and $I(\overline{r})$ is defined as

$$I(\overline{r}) = \frac{i}{8\pi^2 k_0 \frac{z}{r}} e^{i\Phi(k_0 \frac{x}{r}, k_0 \frac{y}{r})} \int_{-\infty}^{\infty} \int_{-\infty}^{\infty} dk_x dk_y e^{\frac{ir}{2k_0 z^2} \left(-(x^2+z^2)k_x^2 + 2xy k_x k_y - (y^2+z^2)k_y^2 \right)} \tag{4.56}$$

The analytic expression for $I(\overline{r})$ is yet to be found. Changing the integration variables with $\tilde{k}_x = \sqrt{\frac{ir}{2k_0 z^2}} k_x$ and $\tilde{k}_y = \sqrt{\frac{ir}{2k_0 z^2}} k_y$, we further obtain

$$I(\overline{r}) = \frac{z}{4\pi^2} e^{ik_0 r} \int_{-\infty}^{\infty} \int_{-\infty}^{\infty} dk_x dk_y e^{\left(-(x^2+z^2)k_x^2 + 2xy k_x k_y - (y^2+z^2)k_y^2 \right)} \tag{4.57}$$

In order to perform the k_y integration, the exponent can be arranged into

$$-(x^2+z^2)k_x^2+2xyk_xk_y-(y^2+z^2)k_y^2 = -(y^2+z^2)(k_y-\frac{xy}{y^2+z^2}k_x)^2-(x^2+z^2-\frac{x^2y^2}{y^2+z^2})k_x^2$$

Therefore, $I(\bar{r})$ becomes

$$I(\bar{r}) = \frac{z}{4\pi^2}e^{ik_0r}\sqrt{\frac{\pi}{y^2+z^2}}\int_{-\infty}^{\infty}dk_x e^{-\frac{(x^2+y^2+z^2)z^2k_x^2}{y^2+z^2}}$$

Eventually, perform the k_x integral to obtain

$$I(\bar{r}) = \frac{z}{4\pi^2}\sqrt{\frac{\pi}{y^2+z^2}}\sqrt{\frac{\pi}{\frac{(x^2+y^2+z^2)z^2}{y^2+z^2}}} = \frac{e^{ik_0r}}{4\pi r}$$

Consequently, the approximated half-space dyadic Green's function is

$$\overline{\overline{G}}_{00}(\bar{r},\bar{r}') = \frac{e^{ik_0r}}{4\pi r}\left\{[\hat{h}(\hat{r})\hat{h}(\hat{r})] + [\hat{v}(\hat{r})\hat{v}(\hat{r})]\right.$$

$$\left.+R^{TE}(k_0\hat{r})e^{ik_0(-\hat{r}^-+\hat{r})\cdot\bar{r}'}[\hat{h}(\hat{r})\hat{h}(\hat{r}^-)] + R^{TM}(k_0\hat{r})e^{ik_0(-\hat{r}^-+\hat{r})\cdot\bar{r}'}[\hat{v}(\hat{r})\hat{v}(\hat{r}^-)]\right\}e^{-ik_0\hat{r}\cdot\bar{r}'}$$

(4.58)

This expression for the dyadic Green's function is indeed the far-field approximation identified by the spherical wave term, $\frac{e^{ik_0r}}{4\pi r}$. The terms in (4.58) state that the main contributions in the propagator are the direct propagation towards the observation direction and the direct reflection into the observation direction.

4.4.3 Single Slush Contribution and Scattered Field

We already have the expression for the half-space dyadic Green's function in (4.58) . Hence, an expression for the scattered field can be obtained from the volume integral equation and the infinite layer approximation in Chapter 4. Here, let k be the wave

57

number of the air.

Under the stationary-phase approximation above, the scattered field is

$$\overline{E}_S(\overline{r}) = k^2 \frac{e^{ikr}}{4\pi r} \left\{ [\hat{h}(\hat{r})\hat{h}(\hat{r})] + [\hat{v}(\hat{r})\hat{v}(\hat{r})] \right\} \cdot \int_V d\overline{r}'(\epsilon_r(\overline{r}') - 1)e^{-ik_0\hat{r}.\overline{r}'}\overline{E}_{int}(\overline{r}')$$

$$+ \left\{ R^{TE}(k_0\hat{r})[\hat{h}(\hat{r})\hat{h}(\hat{r}^-)] + R^{TM}(k_0\hat{r})[\hat{v}(\hat{r})\hat{v}(\hat{r}^-)] \right\} \cdot \int_V d\overline{r}'(\epsilon_r(\overline{r}') - 1)e^{-ik_0\hat{r}^-.\overline{r}'}\overline{E}_{int}(\overline{r}')$$

$$(4.59)$$

Recall that the internal field $\overline{E}_{int}(\overline{r})$ is found to be

$$\overline{E}_{int}(\overline{r}') \approx \left[\left(A\hat{v}(\overline{k_{i1}^-})\hat{v}(\overline{k}_i) + \frac{k_i}{k_1}C\hat{v}(\overline{k_{i1}^-})\hat{v}(\overline{k}_i) \right) e^{i\overline{k_{i1}^-}.\overline{r}'} \right.$$

$$\left. + \left(B\hat{v}(\overline{k_{i1}^+})\hat{v}(\overline{k}_i) + \frac{k_i}{k_1}D\hat{v}(\overline{k_{i1}^+})\hat{v}(\overline{k}_i) \right) e^{i\overline{k_{1i}^+}.\overline{r}'} \right] \cdot \overline{E}_{i0}.$$

In the previous growth process, we denote the positions of slush units by $\overline{r}_m$, $m = 1, \cdots, N$, where N is the number of the building blocks or slush units used to achieve a slush coverage. Though, note that $z_m = 0$ since we only displace slush units on the two-dimensional interface. Hence, the expression in (4.59) is rewritten as

$$\overline{E}_S(\overline{r}) = \frac{k^2 e^{ikr}}{4\pi r} \left[\sum_{m=1}^N e^{i(\overline{k}_i - k\hat{r}).\overline{r}_m} \right] \left[\left\{ [\hat{h}(\hat{r})\hat{h}(\hat{r})] + [\hat{v}(\hat{r})\hat{v}(\hat{r})] \right\} \right.$$

$$\cdot \int_{V_0} d\overline{r}'(\epsilon_r(\overline{r}') - 1)e^{-ik_0\hat{r}.\overline{r}'}\overline{E}_{int}(\overline{r}')$$

$$+ \left\{ R^{TE}(k_0\hat{r})[\hat{h}(\hat{r})\hat{h}(\hat{r}^-)] + R^{TM}(k_0\hat{r})[\hat{v}(\hat{r})\hat{v}(\hat{r}^-)] \right\}$$

$$\left. \cdot \int_{V_0} d\overline{r}'(\epsilon_r(\overline{r}') - 1)e^{-ik_0\hat{r}^-.\overline{r}'}\overline{E}_{int}(\overline{r}') \right]$$

$$(4.60)$$

where V_0 is the volume of the slush unit positioned at the origin.

The only part that depends on the configuration of slush positions $\overline{r}_m$ in (4.60) is the factor $\sum_{m=1}^N e^{i(\overline{k}_i - k\hat{r}).\overline{r}_m}$. Therefore, under the stationary phase approximation, our

expression for the scattered field can be simplified into the product of a configuration factor and the single-unit contribution.

Since we need to generate the most variety of the slush coverage to ensure correct ensemble averages, the slush unit is chosen to be as small as possible up to a number of constraints including the validity of results and computational resources and efficiency. Thus, a slush cover is composed of many slush units in the simulation process. As a result, the ability to calculate the total scattered field by only calculating the single-unit contribution and a simple sum of phases can reduce the numerical complexity tremendously.

However, the stationary-phase approximation for the scattering from one slush may not be accurate enough. The near-field effect should be included for a better prediction of the scattering model. But we still can use the conclusion from stationary-phase approach that the overall scattered field is the product of the scattered field from one slush times the structure factor. Here, we postulate the following when the observation is in the far-field range.

$$\overline{E}_S(\overline{r}) \approx \left[\sum_{m=1}^{N} e^{i(\overline{k}_i - \overline{k}_S) \cdot \overline{r}_m} \right] \cdot \overline{E}_{S1}(\overline{r}) \tag{4.61}$$

where $\overline{r}_m$ is position of slush m and $\overline{E}_{S1}$ is the scattered field from one slush located at the origin[2]. In (4.61) , $\overline{E}_{S1}$ is calculated from numerical inetgral over k_x and k_y, which is different from stationary-phase approach in (4.60) . However, since (4.61) results from the far-field expression in (4.60) , the approximation in (4.61) is also under the assumption that the multiple-scattering effect is negligible. Thus, by using (4.61) , we do not consider the scattered field from one slush induced by the scattered field from another slush.

---

[2]Although, for the stationary-phase expression, the single-slush contribution at the origin differs from that at another place on sea ice by a phase which depends merely on the relative position, the disparity is complicated for the exact expression.

Chapter 5

Monte Carlo Simulation Results

5.1 Backscattering Coefficients

For an incident field $E_{i\beta}$ of β polarization and the scattered field $E_{s\alpha}$ of α polarization, the backscattering coefficient $\sigma_{\alpha\beta}$ is defined as[19]

$$\sigma_{\alpha\beta} = \lim_{r \longrightarrow \infty} \frac{4\pi r^2 |E_{s\alpha}|^2}{A|E_{i\beta}|^2} \tag{5.1}$$

where r is the observation distance and A is the illuminated area.

In the Monte Carlo simulation, for each realization, the model will consist of a finite number of slush patches with known positions. However, the locations of slush patches will vary among different realizations. Each model realization used to calculate the scattered field is generated in the process described in Chapter 3.

The backscattering coefficients will be calculated for many realizations and averaged to obtain the ensemble averages which are the expected simulation values. Besides averaging over various slush unit configurations, we calculate the backscattering coefficients over many azimuthal angles which diversify the ensemble given a fixed slush coverage and fixed angle of incidence. With the rectangular slush unit we

have exploited, the scattering problem obviously does not have the azimuthal symmetry; therefore, the azimuthal consideration is essential for the ensemble average.

5.2 Simulation Parameters

Table 5.1 shows the simulation parameters used in the simulation of the time-series backscattering data. Apart from the scattering angle, the parameters are of physical measurements or their derivatives from all the stages of frost flower growth, where the permittivities are calculated from the mixing formulas given in Chapter 3. The information about salinities is transformed into relative permittivities which are relevant to their use in calculating the scattered field. Only the areal coverage is used for the generation of slush configurations; therefore, it is the only physical measurements which effects the ensemble and the averaging process.

5.3 Results

The developed frost flower covered saline ice scattering model will be validated through the comparison with experimental measurements. The data set used is a time series measurements of the backscattering coefficients at 25 and 35 degrees. The radar backscatter was measured at approximately 6-hour intervals throughout the 3-day period of the experiment [1]. At those angles, the co-polarized backscattering coefficients increased with time except for a sharp fall to the minimum around the 32nd hour. This specific time has been found to coincide with a sharp rise in the surface salinity.

The simulation results compared with the experimental observations are shown in Figure 5-1. The goal of this part of study is to interpret the time series of data at each angle of observation, especially the observed minima and the trend. The sharp rise in
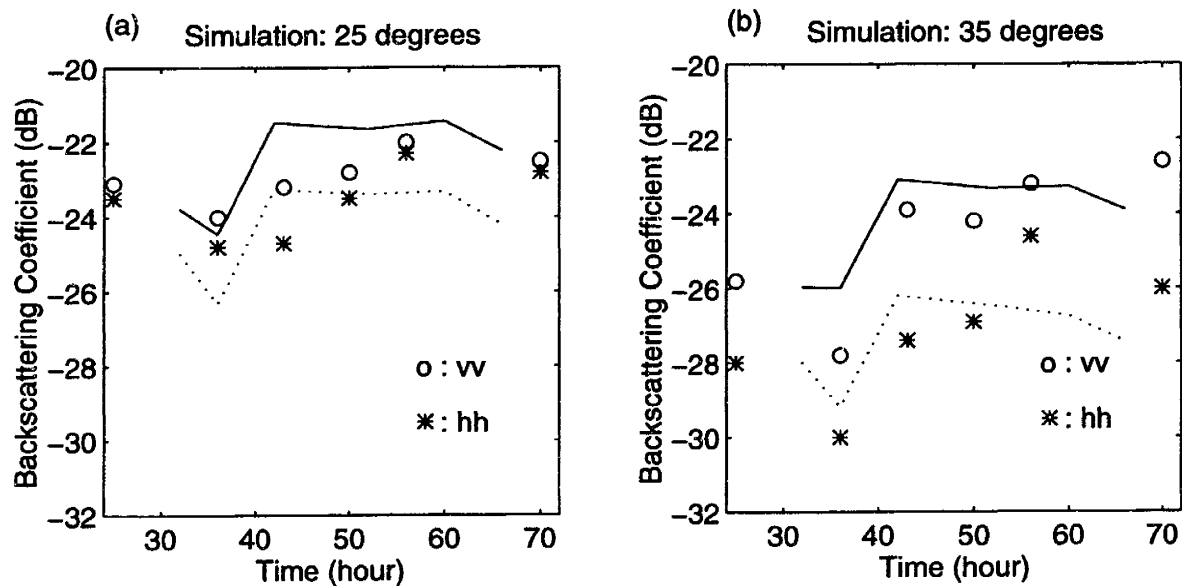
Figure 5-1: The time-series simulation results of the backscattering coefficients compared with the experimental measurements. The isolated points are experimental measurements; the continuous lines are the simulation results. Circles indicate σ_{vv} and stars indicate σ_{hh}. The full line indicates σ_{vv} and the dotted line indicate σ_{hh}.

the surface salinity is an important factor of the well-observed minima. Furthermore, the physical conditions like temperature and salinity will affect the electromagnetic properties of ice, such as the permittivity.

As a result, the levels of simulation results agree with the levels of the experimental data. The simulation results exhibit the fact that σ_{vv} has observed higher than σ_{hh}. Moreover, the local minima are observed in the simulation results and coincide with the experimental results. The minima can be related to the minimum salinity difference between the slush patch and the surface when the surface salinity abruptly changes. In addition, the co-polarized ratios are shown at each incident angle in Table 5.2. The experimental and simulation values agree within 1 dB.

Elapsed time(hr)	Areal coverage(%)	Slush thickness(mm)	ϵ_{slush}	$\epsilon_{surface}$	ϵ_{water}
32	20	1.0	12.48+9.32i	5.43+1.24i	60.3+41.0i
36	40	1.0	14.02+11.36i	9.22+5.15i	60.3+41.0i
42	60	1.5	16.57+14.79i	9.22+5.15i	60.3+41.0i
52	80	2.0	17.25+15.71i	9.22+5.15i	60.3+41.0i
60	85	2.5	17.25+15.71i	9.22+5.15i	60.3+41.0i
66	90	3.0	17.25+15.71i	9.22+5.15i	60.3+41.0i

Table 5.1: Simulation parameters in time series

Co-Polarized	Incident Angles	
Ratio	25°	35°
Experimental Values	1.0 dB	2.8 dB
Simulation Values	2.0 dB	3.5 dB

Table 5.2: The co-polarized ratios at 25 and 35 degrees. The experimental data are for slush patches exposed by removing flower ice crystals in the frost flower formation(about 90% in areal coverage). The simulation values are the calculated results at the areal coverage of 90%.

Chapter 6

Summary

A laboratory experiment at the Geophysical Research Facility in the Cold Regions Research and Engineering Laboratory was conducted during February 1995 to investigate the characteristics of radar backscatter from thin sea ice covered with frost flowers[29]. Polarimetric C-band radar measurements of the backscatter from the ice were made at approximately 6-hour intervals throughout the 3-day period. The observed backscattering coefficients had a similar nonmonotonic trend for σ_{VV} and σ_{HH}, where the coefficient σ_{VV} is always higher than σ_{HH}. Additionally, the observed minima in backscatters were associated with the abrupt increase in the surface salinity occurred early in the flower growth. Furthermore, the radar backscatter of the saline ice covered with frost flowers was 5 dB higher than that of bare ice at the frost flower areal coverage of 90%. At this coverage, the slush patches yielded a backscatter increase of 3-5 dB over that of bare ice. Thus, the experiment has demonstrated that the small ice crystals has little impact on the backscatter.

This thesis develops a theoretical electromagnetic scattering model for sea ice covered with frost flowers. In the part of sea ice, a physical multilayer model is used. The salinity profiles are taken into account to derive the effective permittivity profile by using mixing formulas. For the model of frost flowers, the ice crystals are

neglected due to their small contributions to the backscattering coefficients and the co-polarized ratio. The slush patches are modeled as a thin saline layer composed of an agglomeration of small square slush units of fixed thickness. Thus, initialized with a few seeds, the flower growth is simulated by the accumulation of slush units. With the two-dimensional random walk scheme, a random walk is performed on a new slush unit until it attaches to one of the existing slush patches. Many realizations of the slush coverage are generated to perform the ensemble average for the Monte Carlo simulation.

Due to the high permittivity contrast between the slush patches and sea ice, the volume integral equation approach is used to calculate the scattered field , in which a half-space dyadic Green's function is used to take into account the coupled volume-surface interaction. In the volume integral formulation, the infinite layer approximation is used to estimate the internal field of the slush layer. A simple geometry is used to model the slush unit, and the stationary-phase method is applied to express the total scattered field as the product of the single unit's contribution and a configuration factor. The multiple-scattering effect is, however, ignored in the resulting expression. Thus, the desired simulation results are the ensemble average of the backscattering coefficients which follow directly from the scattered field for each configuration.

The simulation results are compared to the experimental data and match the levels of time-series data well. The scattering model produces higher σ_{vv} backscattering coefficients than σ_{hh} backscattering coefficients. The contribution of saline slush patches to the enhancement of radar backscatter is demonstrated in the simulation results. The simulation values of the co-polarized ratios or the HH-VV difference are close to the measurements. The time variation and trend of the simulation results also follow the similar trend as those of the experimental data. In addition, the

simulation results show the minima which coincide with the observed minima. The observed minimum can be explained by the scattering model in terms of the difference between the surface and slush salinities.

In this study, an electromagnetic scattering model is developed, which successfully describes the polarimetric signatures of saline ice with the presence of frost flowers. The measured backscattering coefficients and co-polarized ratios are imitated by the simulation results with small errors. However, the model can be improved by adopting the ice crystals into the model and by engaging a better computational scheme. For instance, using the same volume integral equation approach, the slush patches can be discretized and solved by the method of moments which automatically includes multiple-scattering effects and near-field interactions with the ice surface. Also, the consideration of the ice crystals may reduce the disparity between the simulation results and the measurements.

Appendix A

Free-Space Dyadic Green's Function

From Maxwell's equations, the electric field, $\overline{E}$, satisfies

$$\nabla \times \nabla \times \overline{E} - k^2\overline{E} = i\omega\mu\overline{J} \qquad (A.1)$$

The solution of $\overline{E}$ can be expressed as a convolution integral over current distribution $\overline{J}(\overline{r})$.

$$\overline{E} = i\omega\mu \int d\overline{r'} \overline{\overline{G}}(\overline{r},\overline{r'}) \cdot \overline{J}(\overline{r'}) \qquad (A.2)$$

where $\overline{\overline{G}}(\overline{r},\overline{r'})$ is the free-space dyadic Green's function which satisfies the inhomogeneous wave equation.

$$\nabla \times \nabla \times \overline{\overline{G}}(\overline{r},\overline{r'}) - k^2\overline{\overline{G}}(\overline{r},\overline{r'}) = \overline{\overline{I}}\delta(\overline{r}-\overline{r'}) \qquad (A.3)$$

where $\overline{\overline{I}} = \hat{x}\hat{x} + \hat{y}\hat{y} + \hat{z}\hat{z}$ is the unit dyad and $\delta(\overline{r})$ is the Dirac delta function.

In the Cartesian coordinate system $(\hat{x}, \hat{y}, \hat{z})$, the dyad $\overline{\overline{G}}(\overline{r},\overline{r'})$ can be expressed,

in terms of the dyad basis $\left\{\hat{\alpha}\hat{\beta}|\alpha,\beta=x,y,z\right\}$ as

$$\overline{\overline{G}}(\overline{r},\overline{r}') = \overline{G}^{(x)}(\overline{r},\overline{r}')\hat{x} + \overline{G}^{(y)}(\overline{r},\overline{r}')\hat{y} + \overline{G}^{(z)}(\overline{r},\overline{r}')\hat{z} \qquad (A.4)$$

where

$$\overline{G}^{(x)}(\overline{r},\overline{r}') = (\hat{x}G_{xx} + \hat{y}G_{yx} + \hat{x}G_{zx}) \qquad (A.5)$$

$$\overline{G}^{(y)}(\overline{r},\overline{r}') = (\hat{x}G_{xy} + \hat{y}G_{yy} + \hat{x}G_{zy}) \qquad (A.6)$$

$$\overline{G}^{(z)}(\overline{r},\overline{r}') = (\hat{x}G_{xz} + \hat{y}G_{yz} + \hat{x}G_{zz}) \qquad (A.7)$$

The three vector constituent functions $\overline{G}^{(x)}(\overline{r},\overline{r}')$, $\overline{G}^{(y)}(\overline{r},\overline{r}')$, and $\overline{G}^{(z)}(\overline{r},\overline{r}')$ can be interpreted as the electric fields satisfying the following equations:

$$\nabla \times \nabla \times \overline{G}^{(x)}(\overline{r},\overline{r}') - k^2\overline{G}^{(x)}(\overline{r},\overline{r}') = \hat{x}\delta(\overline{r}-\overline{r}') \qquad (A.8)$$

$$\nabla \times \nabla \times \overline{G}^{(y)}(\overline{r},\overline{r}') - k^2\overline{G}^{(y)}(\overline{r},\overline{r}') = \hat{y}\delta(\overline{r}-\overline{r}') \qquad (A.9)$$

$$\nabla \times \nabla \times \overline{G}^{(z)}(\overline{r},\overline{r}') - k^2\overline{G}^{(z)}(\overline{r},\overline{r}') = \hat{z}\delta(\overline{r}-\overline{r}') \qquad (A.10)$$

By taking the divergence on both sides of (A.3) , the divergence of the curl vanishes, we have

$$\nabla \cdot \overline{\overline{G}} = -\frac{1}{k^2}\nabla\delta(\overline{r}-\overline{r}') \qquad (A.11)$$

Again, in terms of the vector contituent functions, we have

$$\nabla \cdot \overline{G}^{(x)}(\overline{r},\overline{r}') = -\frac{1}{k^2}\frac{\partial}{\partial x}\delta(\overline{r}-\overline{r}') \qquad (A.12)$$

$$\nabla \cdot \overline{G}^{(y)}(\overline{r},\overline{r}') = -\frac{1}{k^2}\frac{\partial}{\partial y}\delta(\overline{r}-\overline{r}') \qquad (A.13)$$

$$\nabla \cdot \overline{G}^{(z)}(\bar{r}, \bar{r}') = -\frac{1}{k^2} \frac{\partial}{\partial z} \delta(\bar{r} - \bar{r}') \qquad (A.14)$$

Using (A.12) - (A.14) and the identity $\nabla \times \nabla \times = \nabla \nabla \cdot - \nabla^2$, equations (A.8) - (A.10) become

$$(\nabla^2 + k^2)\overline{G}^{(x)}(\bar{r}, \bar{r}') = -(\hat{x} + \frac{1}{k^2}\nabla\frac{\partial}{\partial x})\delta(\bar{r} - \bar{r}') \qquad (A.15)$$

$$(\nabla^2 + k^2)\overline{G}^{(y)}(\bar{r}, \bar{r}') = -(\hat{y} + \frac{1}{k^2}\nabla\frac{\partial}{\partial y})\delta(\bar{r} - \bar{r}') \qquad (A.16)$$

$$(\nabla^2 + k^2)\overline{G}^{(z)}(\bar{r}, \bar{r}') = -(\hat{z} + \frac{1}{k^2}\nabla\frac{\partial}{\partial z})\delta(\bar{r} - \bar{r}') \qquad (A.17)$$

Recall that the scalar Green's function, $g(\bar{r}, \bar{r}')$, satisfying

$$(\nabla^2 + k^2)g(\bar{r}, \bar{r}') = -\delta(\bar{r} - \bar{r}') \qquad (A.18)$$

By comparing (A.15) - (A.17) with (A.18), we have

$$\overline{G}^{(x)}(\bar{r}, \bar{r}') = (\hat{x} + \frac{1}{k^2}\nabla\frac{\partial}{\partial x})g(\bar{r}, \bar{r}') \qquad (A.19)$$

$$\overline{G}^{(y)}(\bar{r}, \bar{r}') = (\hat{y} + \frac{1}{k^2}\nabla\frac{\partial}{\partial y})g(\bar{r}, \bar{r}') \qquad (A.20)$$

$$\overline{G}^{(z)}(\bar{r}, \bar{r}') = (\hat{z} + \frac{1}{k^2}\nabla\frac{\partial}{\partial z})g(\bar{r}, \bar{r}') \qquad (A.21)$$

Substituting (A.19) - (A.21) into (A.4), the free-space dyadic Green's function is expressed as

$$\overline{\overline{G}}(\bar{r}, \bar{r}') = (\overline{\overline{I}} + \frac{1}{k^2}\nabla\nabla)g(\bar{r}, \bar{r}') \qquad (A.22)$$

Appendix B

Spectral Representation of the Free-Space Dyadic Green's Function

The dyadic Green's function $\overline{\overline{G}}(\overline{r}, \overline{r}')$ can be expressed in terms of the scalar Green's function as[1]

$$\overline{\overline{G}}(\overline{r}, \overline{r}') = \left[\overline{\overline{I}} + \frac{1}{k^2} \nabla\nabla \right] g(\overline{r}, \overline{r}') \qquad (B.1)$$

where $k = \frac{2\pi}{\lambda}$ is the wavenumber of free space, and

$$g(\overline{r}, \overline{r}') = \frac{e^{ik_0|\overline{r}-\overline{r}'|}}{4\pi|\overline{r} - \overline{r}'|} \qquad (B.2)$$

The Fourier transform pairs of $g(\overline{r})$ and $G(\overline{k})$ are

$$g(\overline{r}) = \frac{1}{(2\pi)^3} \int \int \int_{-\infty}^{\infty} d\overline{k} \, e^{i\overline{k}.\overline{r}} G(\overline{k}) \qquad (B.3)$$

---

[1]See appendix A

and

$$G(\overline{k}) = \frac{1}{k^2 - k_0^2} \qquad (B.4)$$

where $d\overline{k} = dk_x dk_y dk_z$. Substituting (B.4) into (B.3) , we have

$$g(\overline{r}) = \frac{1}{(2\pi)^3} \int \int \int_{-\infty}^{\infty} d\overline{k} \frac{e^{i\overline{k}.\overline{r}}}{k^2 - k_0^2} \qquad (B.5)$$

To integrate (B.5) over k_z, equation (B.5) can be rewritten as

$$g(\overline{r}) = \frac{1}{(2\pi)^3} \int d\overline{k}_T e^{i\overline{k}_T.\overline{r}_T} \int dk_z \frac{e^{ik_z z}}{k_z^2 - (k_0^2 - k_T^2)} \qquad (B.6)$$

where $d\overline{k}_T = dk_x dk_y$, $\overline{k}_T = k_x \hat{x} + k_y \hat{y}$, $\overline{r}_T = x\hat{x} + y\hat{y}$, and $k_T^2 = k_x^2 + k_y^2$.

Let $k_{0z}^2 = k_0^2 - k_T^2$, the two poles of the integrand of the equation (B.6) are at $\pm k_{0z}$. The integration with respect to k_z in (B.6) can be performed by using the contour integration method. Figure B-1 shows how the contour integration is chosen by considering the convergence of the k_z-integral itself. For $z > 0$, the upper half of the complex k_z-plane is closed by an infinite semi-circular contour running in the positive sense; for $z < 0$, the lower half of the complex k_z-plane is closed by an infinite semi-circular contour running in the negative sense. Hence, we obtain

$$g_{\pm}(\overline{r}) = T(\overline{k}) e^{i\overline{k}_0^{\pm}.\overline{r}} \qquad (B.7)$$

for $\pm z > 0$, where $T(\overline{k})$ and $\overline{k}_0^{\pm}$ are defined as, respectively

$$T(\overline{k}) = \frac{i}{8\pi^2} \int \int_{-\infty}^{\infty} dk_x dk_y \frac{1}{k_{0z}} \qquad (B.8)$$

$$\overline{k}_0^{\pm} = \hat{x} k_x + \hat{y} k_y \pm \hat{z} k_{0z} \qquad (B.9)$$

With the time dependence of $e^{-i\omega t}$, $e^{i\overline{k}_0^{+}.\overline{r}}$ and $e^{i\overline{k}_0^{-}.\overline{r}}$ represent an upward-going and a
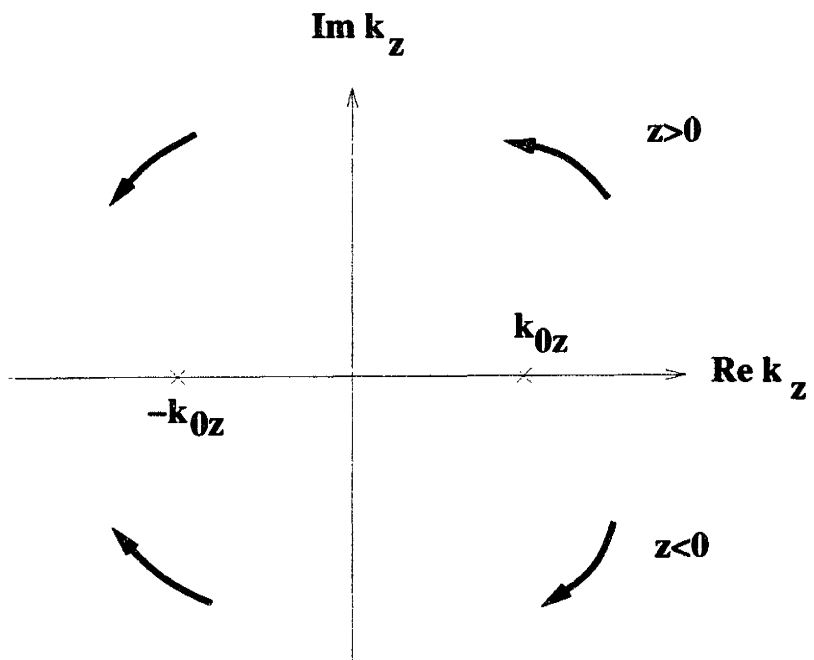
73

Figure B-1: Diagram of the complex regions of the k_z contour integration scheme

downward-going wave, respectively. For $z \neq 0$, the first derivative of $y(\bar{r})$ with respect to z is.

$$\frac{\partial}{\partial z} g_\pm(\bar{r}) = T(\bar{k})(\pm i k_{0z}) e^{i \overline{k_0^\pm} \cdot \bar{r}} \qquad (B.10)$$

Equation (B.10) shows the discontinuity of the first derivative of $g(\bar{r})$. However, we can obtain an expression for the sum of the second-order partial derivatives with respect to x and y,

$$\left(\frac{\partial^2}{\partial x^2} + \frac{\partial^2}{\partial y^2} \right) g(\bar{r}) = T(\bar{k})(-k_T^2) e^{i \overline{k_0^\pm} \cdot \bar{r}}$$

for $\pm z > 0$. BY adding k_0^2 on both sides of equation (B.10), it becomes

$$\left(\frac{\partial^2}{\partial x^2} + \frac{\partial^2}{\partial y^2} + k_0^2 \right) g(\bar{r}) = T(\bar{k})(-k_{0z}^2) e^{i \overline{k_0^\pm} \cdot \bar{r}} \qquad (B.11)$$

for $\pm z > 0$. BY using (B.11) and the equation $(\nabla^2 + k_0^2) g(\bar{r}) = -\delta(\bar{r})$, we get

$$\frac{\partial^2}{\partial z^2} g(\bar{r}) = -\delta(\bar{r}) - T(\bar{k})(k_{0z}^2) e^{i \overline{k_0^\pm} \cdot \bar{r}} \qquad (B.12)$$

for $\pm z > 0$. (B.12) can be easily extended to

$$\frac{\partial^2}{\partial z^2} g(\bar{r} - \bar{r}') = -\delta(\bar{r} - \bar{r}') - T(\bar{k})(k_{0z}^2) e^{i \overline{k_0^\pm} \cdot (\bar{r} - \bar{r}')} \qquad (B.13)$$

for $\pm (z - z') > 0$.

From equations (B.13) and (B.6), we can obtain

$$\nabla \nabla g(\bar{r} - \bar{r}') = -\hat{z}\hat{z}\delta(\bar{r}, \bar{r}') - T(\bar{k}) \overline{k_0^\pm} \, \overline{k_0^\pm} \, e^{i \overline{k_0^\pm} \cdot (\bar{r} - \bar{r}')} \qquad (B.14)$$

for $\pm (z - z') > 0$.

Substituting (B.14) and (B.0), the desired integral representation of $\overline{\overline{G}}(\bar{r}, \bar{r}')$

75

is

$$\overline{\overline{G}}(\overline{r}, \overline{r}') = -\hat{z}\hat{z}\delta(\overline{r} - \overline{r}') - T(\overline{k}) \left[\overline{\overline{I}} - \hat{k}_0^\pm \hat{k}_0^\pm\right] e^{i\overline{k}^\pm \cdot (\overline{r} - \overline{r}')} \qquad (B.15)$$

for $\pm(z - z') > 0$.

To relate $\overline{\overline{G}}(\overline{r}, \overline{r}')$ with the polarizations, two sets of orthonormal bases $\hat{k}_n^\pm, \hat{h}_n^\pm, \hat{v}_n^\pm$ are constructed for wave polarizations in the medium with wavenumber k_n. $\hat{k}_n^+$ corresponds to the wave propagating in the positive z-direction, and $\hat{k}_n^-$ corresponds to the wave propagating in the negative z-direction. This basis is especially convenient for a stratified medium in the z-direction, where the phase-matching condition forces k_x and k_y, the x and y components of the propagation vector, to remain fixed throughout the medium. Figure B-2 shows how the constructed family of bases fit in a stratified medium.

The expressions of $\hat{k}_n^\pm, \hat{h}_n^\pm, and \hat{v}_n^\pm$ are

$$\hat{k}_n^\pm = \frac{1}{k_n}(\hat{x}k_x + \hat{y}k_y \pm \hat{z}k_{nz}) \qquad (B.16)$$

with $k_{nz} = \sqrt{k_n^2 - k_x^2 - k_y^2}$,

$$\hat{h}_n^\pm = \frac{\hat{z} \times \hat{k}_n^\pm}{|\hat{z} \times \hat{k}_n^\pm|} \qquad (B.17)$$

$$\hat{v}_n^\pm = \hat{k}_n^\pm \times \hat{h}_n^\pm \qquad (B.18)$$

and

$$\overline{\overline{I}} - \hat{k}_n^\pm \hat{k}_n^\pm = \hat{h}_n^\pm \hat{h}_n^\pm + \hat{v}_n^\pm \hat{v}_n^\pm \qquad (B.19)$$

In terms of (B.16) - (B.19) , the free-space dyadic Green's function can be
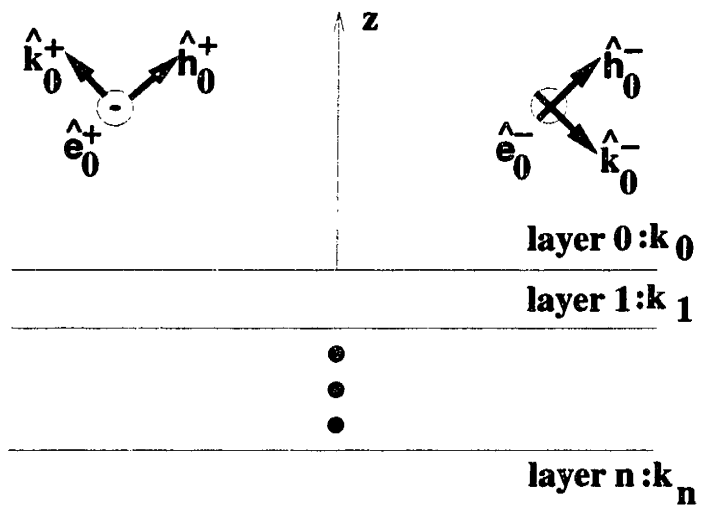
Figure B-2: Illustration: the orientation of basis elements for the wave polarization in a stratified medium

expressed in the form

$$\overline{\overline{G}}(\overline{r}, \overline{r}') = -\hat{z}\hat{z}\delta(\overline{r} - \overline{r}') - T(\overline{k}) \left\{ [\hat{h}_0^{\pm} e^{i\overline{k}^{\pm}\cdot\overline{r}}][\hat{h}_0^{\pm} e^{-i\overline{k}^{\pm}\cdot\overline{r}'}] + [\hat{v}_0^{\pm} e^{i\overline{k}^{\pm}\cdot\overline{r}}][\hat{v}_0^{\pm} e^{-i\overline{k}^{\pm}\cdot\overline{r}'}] \right\} \quad (B.20)$$

for $\pm(z - z') > 0$, where $T(\overline{k})$ is defined in (B.7) .

Appendix C

Half-Space Dyadic Green's Function

By virtue of the fact that each layer is homogeneous and plane-stratified, it is possible to generate from the free-space dyadic Green's function the half-space dyadic Green's function by using the method of scattering superposition[36].

When the observation point $\bar{r}$ is in the region 0, the field must consist of both upward-going (reflected) and downward-going (incident) waves. Thus, the dyadic Green's function $\overline{\overline{G}}_{00}(\bar{r}$ has the following form

$$\overline{\overline{G}}_{00}(\bar{r}, \bar{r}') = T(\bar{k}) \left\{ [\hat{h}_0^- e^{i\overline{k_0^-} \cdot \bar{r}} + R^{TE} \hat{h}_0^+ e^{i\overline{k_0^+} \cdot \bar{r}}][\hat{h}_0^- e^{-i\overline{k_0^-} \cdot \bar{r}'}] \right.$$

$$\left. + [\hat{v}_0^- e^{i\overline{k_0^-} \cdot \bar{r}} + R^{TM} \hat{v}_0^+ e^{i\overline{k_0^+} \cdot \bar{r}}][\hat{v}_0^- e^{-i\overline{k_0^-} \cdot \bar{r}'}] \right\} \qquad (C.1)$$

for $z > z'$. Here R^{TE} and R^{TM} are Fresnel reflection coefficients to be determined by the boundary conditions. The dyadic Green's function $\overline{\overline{G}}_{10}(\bar{r}, \bar{r}')$ in the region 1 has the form:

$$\overline{\overline{G}}_{10}(\overline{r}, \overline{r}') = T(\overline{k}) \left\{ [T^{TE} \hat{h}_0^- e^{i\overline{k_1^-} \cdot \overline{r}}][\hat{h}_0^- e^{-i\overline{k_0^-} \cdot \overline{r}'}] + [T^{TM} \hat{v}_0^- e^{i\overline{k_1^-} \cdot \overline{r}}][\hat{v}_0^- e^{-i\overline{k_0^-} \cdot \overline{r}'}] \right\} \quad (C.2)$$

for $z < z'$.

Here T^{TE} and T^{TM} are Fresnel transmission coefficients to be determined by the boundary conditions as well.

The boundary conditions are the continuity of the tangential components of the electric and magnetic fields at the interface at z=0:

$$\hat{z} \times \overline{\overline{G}}_{00}(\overline{r}, \overline{r}') = \hat{z} \times \overline{\overline{G}}_{10}(\overline{r}, \overline{r}') \quad (C.3)$$

$$\hat{z} \times \nabla \times \overline{\overline{G}}_{00}(\overline{r}, \overline{r}') = \hat{z} \times \nabla \times \overline{\overline{G}}_{10}(\overline{r}, \overline{r}') \quad (C.4)$$

The boundary condition in (C.3) yields

$$\hat{z} \times (\hat{h}_0^- + R^{TE} \hat{h}_0^+) = \hat{z} \times (T^{TE} \hat{h}_1^-) \quad (C.5)$$

for the component perpendicular to the plane of incidence, and

$$\hat{z} \times (\hat{v}_0^- + R^{TM} \hat{v}_0^+) = \hat{z} \times (T^{TM} \hat{v}_1^-) \quad (C.6)$$

for the component in the plane of incidence.

From the facts that $\hat{h}_n^+$ and $\hat{h}_n^-$ are identical for n=0, 1,

$$\hat{h}_n^\pm = -\frac{1}{\sqrt{k_x^2 + k_y^2}}(\hat{x}k_y - \hat{y}k_x)$$

and that

$$\hat{z} \times \hat{v}_n^+ = -\hat{z} \times \hat{v}_n^- = -\frac{k_{nz}}{\sqrt{k_x^2 + k_y^2}k_n}(-\hat{x}k_y + \hat{y}k_x)$$

the equations (C.5) and (C.6) are reduced into

$$T^{TE} = 1 + R^{TE}$$

$$T^{TM} = \frac{k_{0z}}{k_{1z}}\frac{k_1}{k_0}(1 - R^{TM})$$

Similarly, the other boundary condition (C.0) yields

$$\hat{z} \times (\overline{k_0^-} \times \hat{h}_0^- + R^{TE}\overline{k_0^+} \times \hat{h}_0^+) = \hat{z} \times (T^{TE}\overline{k_1^-} \times \hat{h}_1^-) \qquad (C.7)$$

for the component perpendicular to the plane of incidence and

$$\hat{z} \times (\overline{k_0^-} \times \hat{v}_0^- + R^{TM}\overline{k_0^+} \times \hat{v}_0^+) = \hat{z} \times \overline{k_1^-} \times T^{TM}\overline{k_1^-} \times \hat{v}_0^-, \qquad (C.8)$$

for the component in the plane of incidence.

From the fact that

$$\hat{k}_n^\pm \times \hat{h}_n^\pm = \hat{v}_n^\pm \qquad (C.9)$$

the equations (C.7) and (C.8) are reduced to

$$-T^{TE} = \frac{k_{0z}}{k_{1z}}(R^{TE} - 1) \qquad (C.10)$$

$$T^{TM} = \frac{k_0}{k_1}(R^{TM} + 1) \qquad (C.11)$$

Thus, the solutions for the reflection and transmission coefficients are

81

$$R^{TE} = \frac{k_{0z} - k_{1z}}{k_{0z} + k_{1z}} \tag{C.12}$$

$$R^{TM} = \frac{k_1^2 k_{0z} - k_0^2 k_{1z}}{k_1^2 k_{0z} + k_0^2 k_{1z}} = \frac{\epsilon_1 k_{0z} - \epsilon_0 k_{1z}}{\epsilon_1 k_{0z} + \epsilon_0 k_{1z}} \tag{C.13}$$

$$T^{TE} = \frac{2k_{0z}}{k_{0z} + k_{1z}} \tag{C.14}$$

$$T^{TM} = \frac{2k_0 k_1 k_{0z}}{k_1^2 k_{0z} + k_0^2 k_{1z}} \tag{C.15}$$

The coefficients exactly coincide with the reflection and transmission coefficients in the treatment of a plane wave incidence on the interface of a half-space medium. Furthermore, the fact reassures that the derivation of the expansion of the half-space dyadic Green's function from the spectral expansion of the free-space dyadic Green's function. From this observation, it can be verified that the integral expression for the dyadic Green's function is indeed the spectral expansion of the dyadic Green's function. The operation of the dyadic Green's function on each frequency component of a wave appears clearly in the integrand up to a factor of $\frac{1}{k_{0z}^2}$. The spectral expansion is two-dimensional because the wavenumbers only depend on the property of the medium and are fixed. Thus, only the direction of the propagation vector can be freely specified and doing so takes two angular parameters.

Bibliography

[1] S.A. Arcone, A.J. Gow, and S. McGrew. Microwave dielectric, structural, and salinity properties of simulated sea ice. *Trans. Geosci. Remote Sensing*, GE-24(6):832, 1986.

[2] F. D. Carsey, editor. *Microwave Remote Sensing of Sea Ice*. American Geophysical Union, 1992.

[3] W.C. Chew. *Waves and Fields in Inhomogeneous Media*. IEEE PRESS, New York, 1995.

[4] S.K. Cho. *Electromagnetic Scattering*. Springer-Verlag, New York, 1990.

[5] P. Coutu. Radiative transfer theory for active remote sensing of sea ice. Master's thesis, Massachusetts Institute of Technology, 1993.

[6] G.F.N. Cox and W.F. Weeks. Equations for determining the gas and brine volumes in sea ice samples. *Journal of Glaciology*, 29(102):306, 1983.

[7] J.G. Dash, H. Fu, and J.S. Wettlaufer. The premelting of ice and its environmental consequences. *Rep. Prog. Phys.*, 58:115, 1995.

[8] M.R. Drinkwater and G.B. Crocker. Modelling changes in the dielectric and scattering properties of young snow-covered sea ice at GHz frequencies. *J. Glaciology*, 34:274, 1988.

[9] H. Eicken. Salinity profiles of Antarctic sea ice: field data and model results. *Journal of Geophysical Research*, 97(C10):15,545, 1992.

[10] H. T. Ewe. Radiative transfer theory for active and passive remote-sensing of sea ice. Master's thesis, Massachusetts Institute of Technology, 1994.

[11] A.K. Fung. *Microwave scattering and emission models and their applications.* Artech House, Boston, MA, 1994.

[12] T.C. Grenfell, D.J. Cavalieri, J.C. Comiso, M.R. Drinkwater, R.G. Onstott, I. Rubinstein, K. Steffen, and D.P. Winebrenner. Considerations for microwave remote sensing of thin sea ice. In F.D. Carsey, editor, *Microwave remote sensing of sea ice.* American Geophysical Union, 1992.

[13] D.K. Hall and J. Martinec. *Remote Sensing of Ice and Snow.* Chapman and Hall, New York, 1985.

[14] J. Hallett and B.J. Mason. The influence of temperature and supersaturation on the habit of crystals grown from the vapor. *Proc. R. Soc. London A*, 247:440, 1958.

[15] W. Hallikainen and D.P. Winebrenner. The physical basis for sea ice remote sensing. In F.D. Carsey, editor, *Microwave remote sensing of sea ice.* American Geophysical Union, 1992.

[16] C.C. Hsu. *Theoretical models for microwave remote sensing of forest and vegetation.* PhD thesis, Massachusetts Institute of Technology, 1996.

[17] L. Klein and C. Swift. An improved model for the dielectric constant of sea water at microwave frequencies. *IEEE Trans. Antennas Propagat.*, AP-25:104, 1977.

[18] J.A. Kong. *Electromagnetic Wave Theory.* John Wiley & Sons, Inc., New York, 1986.

[19] S. Martin. A field study of brine drainage and oil entrainment in first-year sea ice. *J.Glaciology*, 22:473, 1979.

[20] S. Martin, R. Drucker, and Meredith Fort. A laboratory study of frost flower growth on the surface of young sea ice. *J.Geophys.*, 100(C/4):7027, 1995.

[21] S. Martin, Y. Yu, and R. Drucker. The temperature dependence of frost flower growth on laboratory sea ice and the effect of the flowers on infrared observations of the surface. *J.Geophys.*, 101(C/5):12111, 1996.

[22] R. Massom. *Satellite Remote Sensing of Polar Region.* Belhave Press, Boca Raton, FL, 1991.

[23] G.A. Maykut. Energy exchange over young sea ice in the central Arctic. *J. Geophys. Res.*, 83(C7):3646, 1978.

[24] M. Nakawo and N.K. Sinha. Growth rate and salinity profile of first-year sea ice in the high Antarctic. *Journal of Glaciology*, 27(96):315, 1981.

[25] S.V. Nghiem, R. Kwok, S.H. Yueh, and M.R. Drinkwater. Polarimetric signature of sea ice, 1. theoretical model. *J. Geophys. Res.*, 100(C7):13665, 1995.

[26] S.V. Nghiem, R. Kwok, S.H. Yueh, A.J. Gow, D.K. Perovich, J.A. Kong, and C.C. Hsu. Evoluation in polarimetric signatures of thin saline ice under constant growth. *Radio Science*, 1997.

[27] S.V. Nghiem, R. Kwok, S.H. Yueh, J.A. Kong, C. Hsu, M.A. Tassoudji, and R.T. Shin. Polarimetric scattering from layered media with multiple species of scatterers. *Radio Science*, 30(4):835, 1995.

[28] S.V. Nghiem, R. Kwok, S.H. Yueh, R. West, S. Martin, R. Drucker, D.K. Perovich, A.J. Gow, J.A. Kong, J.T. Johnson, and K.H. Ding. Polarimetric remote sensing of sea ice: CRRELEX 1995. In *Laboratory studies of the electromagnetic properties of saline ice: year 3 experiments, summary submitted to the office of Naval Research, April 1995*, 1995.

[29] S.V. Nghiem, S. Martin, D.K. Perovich, R. Kwok, R. Drucker, and A.J. Gow. A laboratory study of the effect of frost flowers on c-band radar backscatter from sea ice. *J.Geophys.*, 102(C/2):3357, 1997.

[30] R.G. Onstott. SAR and scatterometer signatures of sea ice. In F.D. Carsey, editor, *Microwave remote sensing of sea ice*. American Geophysical Union, 1992.

[31] D.K. Perovich and J.A. Richter-Menge. Surface characteristics of lead ice. *J.Geophys.*, 99(C/8):16341, 1994.

[32] S.E. Shih, K.H. Ding, S.V. Nghiem, C.C. Hsu, J.A. Kong, and A.K. Jordan. Thickness retrieval using time series electromagnetic measurements of laboratory grown saline ice. In *IGARSS'96 Conference Proceedings*, page 1208. IGARSS, 1996.

[33] S.E. Shih, K.H. Ding, S.V. Nghiem, C.C. Hsu, J.A. Kong, and A.K. Jordan. Thin saline ice thickness retrieval using time series C-band polarimetric radar measurements. *IEEE Trans. Geosci. Remote Sensing*, 1997.

[34] A.H. Sihvola and J.A. Kong. Effective permittivity of dielectric mixtures. *Transactions on Geoscience and Remote Sensing*, 26(4), 1988.

[35] A. Stogryn. Equations for calculating the dielectric constant of saline water. *IEEE Trans. Microwave Theory Tech.*, MTT-19:733, 1971.

[36] C.T. Tai. *Dyadic Green Functions in Electromagnetic Theory, 2nd ed.* IEEE PRESS, Piscataway, NJ, 1994.

[37] L. Tsang, J.A. Kong, and R.T. Shin. *Theory of Microwave Remote Sensing.* John Wiley & Sons, Inc., 1985.

[38] F.T. Ulaby and A.K. Fung. *Microwave Remote Sensing*, volume 3. Artech House, Dedham, 1985.

[39] L.M.H Ulander, A. Carlstroem, and J. Askne. Effect of frost flowers, rough saline snow and slush on the ERS-1 SAR backscatter of thin Arctic sea-ice. *International Journal of remote sensing*, 16(17):3287, 1995.

[40] M.E. Veysoglu. *Direct and inverse scattering models for random media and rough surfaces.* PhD thesis, Massachusetts Institute of Technology, 1994.

[41] M.E. Veysoglu, H.T. Ewe, A.K. Jordan, R.T. Shin, and J.A. Kong. Inversion algorithms for remote sensing of sea ice. In *IGARSS'94 Conference Proceedings*, page 626. IGARSS, 1994.

[42] W. Weeks and S. Ackley. The growth, properties and structure of sea ice. In *US Army CRREL Monograph 82-1.* US Army CRREL, 1982.

[43] M.R. Wensnahan, T.C. Grenfell, D.P. Winebrenner, and G.A. Maykut. Observations and theoretical studies of microwave emission from thin saline ice. *J. Geophys. Res.*, 98(C5):8531, 1993.

[44] D.P. Winebrenner, J. Bredow, A.K. Fung, M.R. Drinkwater, S. Nghiem, A.J. Gow, D.K. Perovich, T.C. Grenfell, H.C. Han, J.A. Kong, J.K. Lee, S. Mudaliar, R.G. Onstott, L. Tsang, and R.D. West. Microwave sea ice signature modeling. In F.D. Carsey, editor, *Microwave remote sensing of sea ice.* American Geophysical Union, 1992.

THESIS PROCESSING SLIP

FIXED FIELD: ill. _____ name _____

index _____ biblio _____

► COPIES: (Archives) Aero Dewey (Eng) Hum

Lindgren Music Rotch Science

TITLE VARIES: ►☑ the word "Saline" is left out of the degree book title

NAME VARIES: ►☐ _____

IMPRINT: (COPYRIGHT) _____

►COLLATION: 95ℓ _____

►ADD. DEGREE: _____ ►DEPT.: _____

SUPERVISORS: _____

NOTES:

cat'r: _____ date: _____

page: ►532

►DEPT: E.E.

►YEAR: 1997 ►DEGREE: M.Eng

►NAME: PIMSAMARN, Kulapant